ANNUAL REVIEWS

Annual Review of Astronomy and Astrophysics

The ALMA View of High-Redshift Galaxy Formation

Renske Smit[1] and Rebecca A.A. Bowler[2]

[1]Astrophysics Research Institute, Liverpool John Moores University, Liverpool, United Kingdom; email: r.smit@ljmu.ac.uk

[2]Jodrell Bank Centre for Astrophysics, Department of Physics and Astronomy, The University of Manchester, Manchester, United Kingdom; email: rebecca.bowler@manchester.ac.uk

Annu. Rev. Astron. Astrophys. 2026. 64:493–535

First published as a Review in Advance on June 25, 2026

The *Annual Review of Astronomy and Astrophysics* is online at astro.annualreviews.org

https://doi.org/10.1146/annurev-astro-052722-104242

Keywords

Galaxies, galaxy evolution, dust, ISM, radio lines: mm, atomic fine-structure lines

Abstract

The advent of routine operations with the Atacama Large Millimeter/submillimeter Array (ALMA) in the past decade has led to a revolution in the direct study of the interstellar medium (ISM) in "normal" high-redshift galaxies in the rest-frame far-infrared (FIR). This review summarizes the observational literature on $z > 6.5$ sources observed with ALMA and NOEMA (NOrthern Extended Millimeter Array). The main findings are as follows:

- Cool gas consistently scales with star formation in a wide range of galaxy environments, similar to local relations, suggesting that fundamental processes of star formation have stayed relatively constant over 13 billion years of cosmic time.
- Significant metal enrichment is present in galaxies just ∼300–400 million years after the Big Bang.
- There is a trend to a higher obscured fraction of star formation with stellar mass and star-formation rate (SFR) already in place at $z \simeq 7$, with measurements of the cosmic SFR density showing that >10% of the SFR density is obscured at this epoch.
- The estimated dust masses compared to the stellar mass suggest that rapid dust enrichment occurs, likely from supernovae with little dust destruction and/or rapid growth in the ISM, which is in agreement with maximal predictions from models.
- In individual sources, cold disks are already in existence, with their gas disks being more extended and smoother than their observed stellar counterparts.

Contents

1. INTRODUCTION

1.1. Background

The earliest stages of galaxy formation and evolution in the first billion years of cosmic time were characterized by the formation of the first stars (generating the first heavy elements and dust grains), the first black holes, and the first galaxies. This was in combination with the Universe-wide phase change called the epoch of reionization (EoR), when the intergalactic medium (IGM) transitioned from being predominantly neutral to ionized (see reviews by Stark 2016, Dayal & Ferrara 2018, Robertson 2022).

In dark energy (Λ) and cold dark matter (ΛCDM) cosmology, many differences between high-redshift galaxy formation and local galaxy evolution are directly linked to the evolution of the underlying dark matter halos across cosmic time. First, the specific accretion rate ($\dot{M}/M$) of dark matter (DM) and gas from the cosmic web onto halos increases steadily toward higher redshift (Somerville & Davé 2015). As a result, the (minor) merger rate, as well as the total gas fractions within galaxies, is expected to increase with redshift. Furthermore, for a given depletion rate of gas into stars, the expected specific star-formation rate (sSFR $=$ SFR$/M_*$) should roughly follow a

EoR: epoch of reionization

IGM: intergalactic medium

ΛCDM: dark energy (Λ) and cold dark matter

DM: dark matter

similar evolution, such that galaxies at $z = 7$ have an $\sim$1.5–2 dex higher star-formation rate (SFR) compared to $z = 0$ galaxies at fixed stellar mass (Stark 2016). The increased accretion rates, as well as the higher SFR and associated stellar feedback per unit mass, are expected to increase the turbulence in the interstellar medium (ISM) (Förster Schreiber & Wuyts 2020). Second, as halos collapse at higher redshift against the denser background of the expanding Universe, it is predicted that the gas that settles into galaxies will be of higher density. Assuming conservation of angular momentum of the gas in the halo as it cools onto a disk, galaxy sizes will scale with the virial radii of the halo, such that $z = 7$ star-forming galaxies are expected to be $\sim 5-8\times$ more compact than their $z = 0$ counterparts at fixed stellar mass (Dayal & Ferrara 2018), further contributing to higher gas and SFR surface density in the early Universe. The combined effect of higher gas fractions and higher turbulence in more compact, denser galaxies increases the ISM pressure and the conditions under which stars form. This in turn leads to more massive star clusters and more massive stars forming, which can have a galaxy-wide impact through their stellar feedback processes (Crain & van de Voort 2023).

ISM: interstellar medium

CMB: cosmic microwave background

ALMA: Atacama Large Millimeter/submillimeter Array

In addition to galaxy evolution effects linked to the cosmic web within the expanding Universe, galaxies in the first billion years are affected by the timescales needed to build up significant metal and dust reservoirs after the first stars form. In particular, asymptotic giant branch (AGB) stars are thought to produce a significant fraction of the dust in our local Universe; however, their timescales spent on the stellar main sequence (MS) ranges from a hundred million to billions of years, allowing for only a minor contribution at very early times (Schneider & Maiolino 2024). As a result, there remain large gaps in our understanding of the rate of dust buildup and the dust grain composition—and resulting dust extinction law—in high-redshift galaxies. Finally, the increasing temperature of the cosmic microwave background (CMB) heats all but the most self-shielded dust regions, impacting gas cooling during the star-formation process (Bate 2025).

Given these dramatic changes from the physical processes at lower redshift, a great number of open questions on high-redshift galaxy formation remain: How early do the first galaxies build up their metal and dust reservoirs? How does the ISM (and circumgalactic medium, i.e., CGM) of these early systems allow for escape of ionizing photons from massive stars into the IGM? Are the local scaling relations that are fundamental to star formation already in place in the first billion years of cosmic time? How is dust obscuration affecting our understanding of the physical properties of early galaxies? Can settled galaxy disks already form or are the majority of early systems dominated by turbulence?

The *James Webb Space Telescope* (JWST) is providing new constraints on the stellar and hot gas properties of galaxies in the EoR. In particular, findings of bursty star-formation histories (SFHs) and an overabundance of luminous galaxies as early as $z = 14$ have been discovered at the time of writing (e.g., Carniani et al. 2024). However, in order to test the current theoretical framework out to the highest redshifts, it is simultaneously critical to constrain the presence and properties of dust and gas—fundamental building blocks of galaxy growth that submillimeter telescopes in the Atacama Large Millimeter/submillimeter Array (ALMA) era are uniquely capable of detecting.

Despite accounting for only 1% of the ISM mass, dust grains not only scatter and absorb starlight and reradiate the absorbed energy as mid-infrared (MIR) aromatic features and thermal FIR continuum but also, within the life cycle of the ISM, facilitate numerous chemical reactions, including the formation of the H_2 molecule, and are responsible for the heating of the gas in photodissociation regions, energetically coupling the stellar radiation field to the gas outside of ionized regions (Galliano et al. 2018). Cosmic gas is mostly comprised of hydrogen in its neutral (HI) and molecular (H_2) phases—the latter is the one most directly associated with star formation, whereas the neutral phase is considered the long-term gas reservoir. The gas and dust properties of galaxies at $z \simeq 7$ are intricately linked with the cosmic reionization process, as the escape of

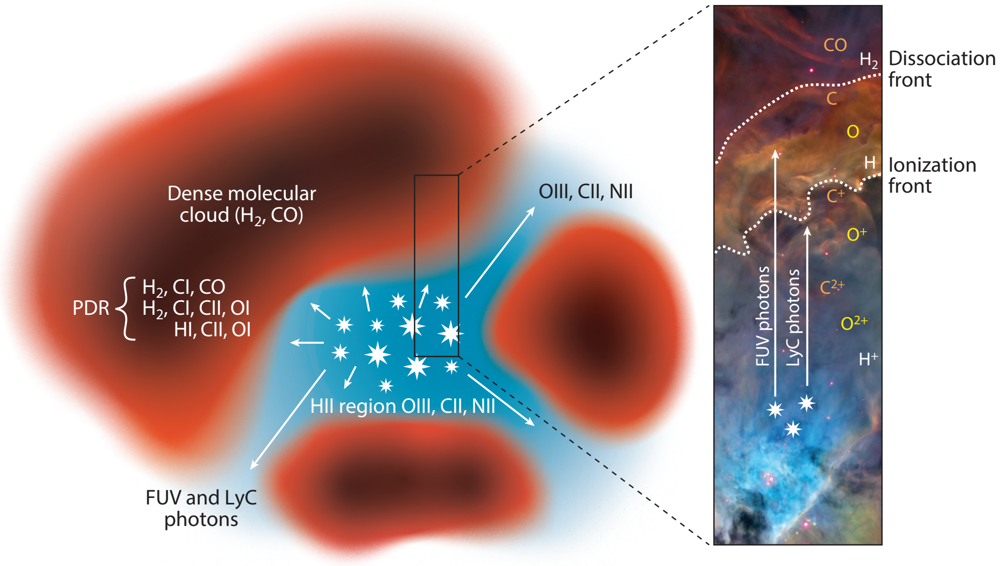

Figure 1

An illustration of the multiphase gas and dust across a galaxy within the epoch of reionization. Young star clusters are shown as the white stars, which ionize HII regions around them. Channels of ionized gas in which Lyman continuum photons escape are also shown. Dense molecular regions are shown in red and black, which are the sites of a significant proportion of the dust grains. The edges of the molecular regions are PDRs, where [CII] is predominantly produced (Wolfire et al. 2022). The complex geometry of the stars, ionized and neutral gas, and dust impacts the multiwavelength properties of galaxies within the EoR. Inset image by Livia Vallini, adapted from NASA/*Hubble*. Abbreviations: FUV, far ultraviolet; LyC, Lyman continuum; PDR, photodissociation region.

ionizing photons from massive stars can be regulated by the properties and geometry of gas and dust surrounding star-forming regions (Dayal & Ferrara 2018, Robertson 2022) (see **Figure 1**).

1.2. Motivation

The past decade, since the commissioning of ALMA in 2014, has seen a revolution in the observations of cold gas and dust within galaxies at very high redshifts. Here, we aim to summarize the current state of the field by creating a compilation of the published ALMA and NOrthern Extended Millimeter Array (NOEMA) observations targeting the $z > 6.5$ population to date,[1] allowing us to summarize the current state of the art and identify the key open questions to be answered in the next decade of ALMA. Our philosophy for this review is to connect the historically relatively separate communities of high-redshift galaxy observations, based on the redshifted rest-frame ultraviolet (UV) light, and detections of dusty sources in the millimeter–submillimeter wavelengths. The key to this is to introduce both the basics of ALMA observing and give an overview of the rest-frame UV selection techniques that are required to select the target sample for follow-up in the submillimeter wavelengths. The detailed properties of the target high-redshift galaxies and quasars from a mainly rest-frame UV/optical standpoint have been presented by Stark (2016), Ouchi et al. (2020), and Fan et al. (2023). We also refer the reader to Robertson (2022) for a review of galaxies contributing to reionization (pre-JWST). We do not discuss in detail

NOEMA: NOrthern Extended Millimeter Array

[1]This redshift was chosen not only to enable a focus on the EoR but also to include the rich datasets that have targeted the interval $z = 6.5$–7.0 (e.g., Reionization Era Bright Emission Line Survey or REBELS).

lower-redshift dusty galaxies or the theoretical background of dust emission; recent reviews on these topics have been written by Hodge & da Cunha (2020), Salim & Narayanan (2020), and Schneider & Maiolino (2024). The review of cold gas emission by Carilli & Walter (2013) summarized the state-of-the-art FIR line emission measurements available prior to ALMA, which included a single source (a quasar host galaxy) at $z > 6.5$. Due to observational limitations, there were no detections of line or continuum emission from more normal galaxies with existing facilities [mainly the Plateau de Bure interferometer (PdBI) at the Institut de Radio Astronomie Millimétrique (IRAM)]. In the context of this review, we define normal galaxies as those with SFRs of $\lesssim 100\,M_{\odot}$ year^{-1} and without active black holes. FIR properties of quasars are discussed by Fan et al. (2023). A complementary review of FIR fine-structure lines is that by Decarli & Díaz-Santos (2025).

In Section 2, we discuss various analysis methods and concepts important for interpreting FIR line and continuum observations obtained through interferometry. In Section 3, we present the compilation of $z > 6.5$ galaxies used in this review, including their selection methods and the largest high-redshift observational ALMA programs that have contributed to the sample. We present an overview of emission lines accessible to ALMA at $z > 6.5$ in Section 4, including their physical interpretation and the observational progress to date. We discuss dust continuum observations and dust buildup in Section 5, whereas we summarize the progress on resolved observations and kinematics in Section 6. Finally, we discuss how ALMA has addressed the questions posed in the previous section and what the future outlook is for ALMA observations in the next decade in Section 7.

2. OBSERVATIONAL METHODS

In this section, we present a summary of the key observational methods used in the detection and study of FIR continuum and line emission in galaxies and quasars at high redshifts. An overview of the multiwavelength continuum and line emission expected from a high-redshift star-forming galaxy is shown in **Figure 2**.

2.1. (Sub)Millimeter Line Observations

Working with line luminosities at (sub)millimeter wavelengths comes with definitions and units that are not typically used in optical/near-infrared (NIR) studies. These differences have emerged owing to historic reasons for the distinctly different observational techniques (Solomon & Vanden Bout 2005, Carilli & Walter 2013), but also owing to differences between the phases of the ISM that are probed, with optical/NIR line studies focusing on the ionized gas (typically HII regions around young star clusters), whereas low-redshift submillimeter line studies have focused on molecular gas. At high redshift, ALMA can now target a variety of phases in galaxies at $z > 6$; from ionized gas (through [OIII], [NII]) to neutral gas ([CII], [OI]), and even molecular gas ([CII], CI, CO). An overview of lines is given in **Table 1** and **Figure 3**. An elaborate discussion of the excitation mechanisms of the different lines, the use of critical density in the submillimeter and optical/NIR literature and the impact of the ionization field on the different gas phases is given in the **Supplemental Text** (see also Decarli & Díaz-Santos 2025).

Supplemental Material >

The submillimeter line luminosity, $L_{\rm line}$ (in $L_{\odot}$), can be derived from the observed flux density as

$$L_{\rm line} = 1.04 \times 10^{-3}\, S_{\rm line} \Delta v\, D_{\rm L}^2\, \nu_0\, (1+z)^{-1}. \qquad 1.$$

Here, $S_{\rm line}\Delta v$ is the velocity integrated line flux in units of Jy km s^{-1}, ν_0 is the rest-frame frequency ($\nu_{\rm obs} = \nu_0\,(1+z)^{-1}$) in gigahertz, and D_L is the luminosity distance in megaparsecs.

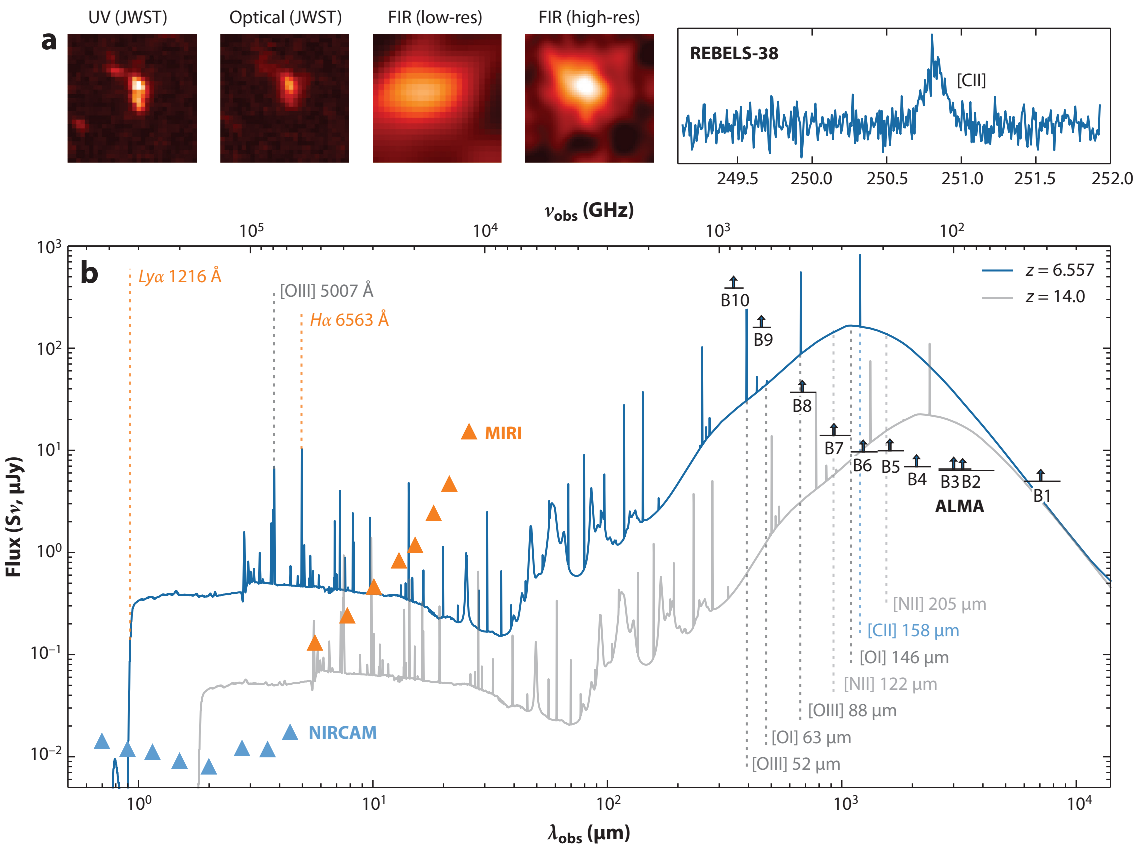

Figure 2

An illustration of the regions of a $z = 7$ galaxy SED observed by different facilities. (*a*) The observed JWST and ALMA data from REBELS-38 are shown on the left, with the [CII] data for this galaxy on the right. (*b*) The best-fit SED model for REBELS-38. SED model taken from Fisher et al. (2025). The wavelength of the ALMA observing bands are shown as the black horizontal lines labeled from bands 1 to 10, and common FIR emission lines are highlighted with the vertical dashed lines. The triangles and arrows, respectively, show the sensitivity achieved by JWST (*blue* and *orange*) and ALMA (*black*) in 10,000 s of observation. Abbreviations: ALMA, Atacama Large Millimeter/submillimeter Array; FIR, far-infrared; JWST, *James Webb Space Telescope*; MIRI, Mid-Infrared Instrument; NIRCam, Near Infrared Camera; SED, spectral energy distribution.

The velocity integrated line flux, $S_{\mathrm{line}}\Delta v$, is almost exclusively used in submillimeter/radio studies and can be converted to cgs (centimeter–gram–second) units of erg s^{-1} cm^{-2} by multiplying with $10^{-14} \cdot \nu_{\mathrm{obs}}/c$, where ν_{obs} is the observed frequency in gigahertz, and c is in km s^{-1}. Note that as a result, the luminosity ratio of two lines, $L_{\mathrm{line1}}/L_{\mathrm{line2}}$, scales as $(S_{\mathrm{line1}}\Delta v)/(S_{\mathrm{line2}}\Delta v) \cdot \nu_{\mathrm{line1}}/\nu_{\mathrm{line2}}$ rather than the direct ratio of the submillimeter line fluxes.

Supplemental Material >

Infrared luminosity, L_{IR}: 8–1,000 μm

Far-infrared luminosity, L_{FIR}: 42.5–122.5 μm

2.2. Dust Continuum Emission

Through heating of the dust grains, the energy from young stars is reradiated in the FIR and observed as a modified blackbody (MBB) form (see **Supplemental Figure 1**). Through assuming a functional form of the spectral energy distribution (SED) in the FIR region, and integrating, the infrared luminosity (L_{IR}) can be determined. Note that different definitions of luminosity in the infrared exist, including the far-infrared luminosity (L_{FIR}) and the total infrared luminosity

Table 1 Parameters for line transitions accessible to ALMA at $z > 6.5$

Species	Transition	λ (μm)	ν (GHz)	Ionization potential (eV)	Excitation potential (K)	n_{crit} (cm^{-3})[a]
PDR/neutral gas						
[CII]	$^2P_{3/2} \rightarrow {}^2P_{1/2}$	157.74	1,900.54	11.3–24.4	91	2.8×10^3
[OI]	$^3P_1 \rightarrow {}^3P_2$	63.18	4,744.77	0–13.6	228	4.7×10^5
	$^3P_0 \rightarrow {}^3P_1$	145.53	2,060.07		329	9.4×10^4
[CI]	$^3P_2 \rightarrow {}^3P_1$	370.42	809.34	0–11.3	63	1.2×10^3
	$^3P_1 \rightarrow {}^3P_0$	609.14	492.16		24	4.7×10^2
CO	$J = 7-6$	371.65	806.65		155	3.9×10^5
	$J = 6-5$	433.56	691.47		116	2.6×10^5
	$J = 5-4$	520.2	576.27		83	1.7×10^5
	$J = 4-3$	650.3	461.04		55	8.7×10^4
	$J = 3-2$	867.0	345.80		33	3.6×10^4
Ionized gas						
[CII]	$^2P_{3/2} \rightarrow {}^2P_{1/2}$	157.74	1,900.54	11.3–24.4	91	50
[OIII]	$^3P_2 \rightarrow {}^3P_1$	51.82	5,785.88	35.1–54.9	440	3.6×10^3
	$^3P_1 \rightarrow {}^3P_0$	88.36	3,393.01		163	510
[NII]	$^3P_2 \rightarrow {}^3P_1$	121.90	2,459.38	14.5–29.6	188	310
	$^3P_1 \rightarrow {}^3P_0$	205.18	1,461.13		70	48
[NIII]	$^2P_{3/2} \rightarrow {}^2P_{1/2}$	57.32	5,230.43	29.6–47.4	251	2.1×10^3

[a]For PDR/neutral gas, the collision partners are H and H_2 (assuming $T_{gas} = 100$ K), whereas for ionized gas the collision partner is electrons (Carilli & Walter 2013).

Abbreviations: ALMA, Atacama Large Millimeter/submillimeter Array; PDR, photodissociation region.

(L_{TIR}). As the majority of $z > 6.5$ sources with ALMA observations have only one continuum band detection or nondetection, in practice a simplified form is used when estimating the L_{IR}. For a detailed overview of dust composition and different dust SEDs, we refer the reader to Draine (2003) and Casey et al. (2014). In the general form, we can model the flux observed at rest-frame frequency ν for a given dust temperature T_d as:

$$S(\nu, T_d) = \frac{(1 - e^{-\tau(\nu)})\nu^3}{e^{h\nu/kT_d} - 1}. \quad 2.$$

Here, the optical depth is given by $\tau(\nu) = (\nu/\nu_0)^{\beta_d} = (\lambda_0/\lambda)^{\beta_d}$, where β_d is the dust spectral emissivity index that depends on the dust composition, and ν_0 (λ_0) is the frequency (wavelength) at which the optical depth equals unity (Draine 2003). Measured values of this wavelength at lower redshift show $\lambda_0 = 50$–200 μm (Simpson et al. 2017). It is typically assumed that the observed fluxes at high redshift with ALMA are at $\lambda > \lambda_0$ such that the dust can be assumed to be optically thin. In the optically thin limit, the function becomes

$$S(\nu, T_d) = \frac{\nu^{(\beta_d+3)}}{e^{h\nu/kT_d} - 1}. \quad 3.$$

Total infrared luminosity, L_{TIR}: 3–1,100 μm

An additional power-law component has been advocated at lower redshifts, as well as multiple temperature components (Casey 2012). However, for observations at $z > 6.5$, where, in the majority of cases, a single band detection or upper limit is obtained, a simple optically thin MBB is typically assumed.

In the limit of a Planck function (with $\beta_d = 0$), the dust temperature is related to the observed peak in the SED via Wien's displacement law with $\lambda_{peak} \propto 1/T_d$. In the case of MBB forms,

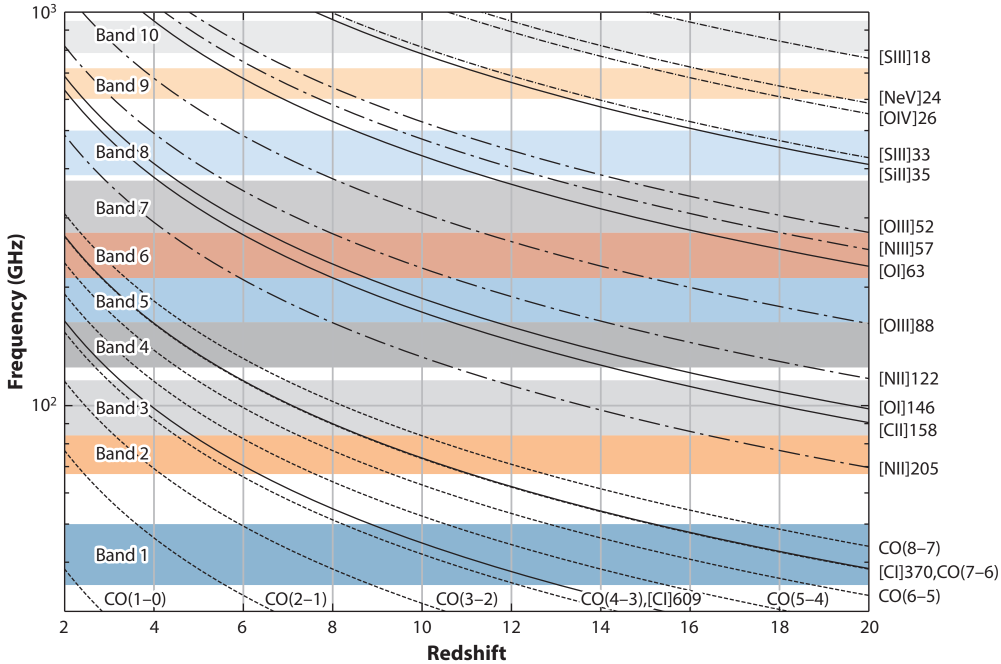

Figure 3

Overview of lines that are accessible with the Atacama Large Millimeter/submillimeter Array at $z = 2{-}20$.

Supplemental Material >

however, the temperature defined by the observed peak in the SED ($T_{\rm peak}$) differs from the dust temperature input into the SED formalism ($T_{\rm SED}$), as is shown in **Supplemental Figure 2**. In this review, we quote $T_{\rm d}$ as the second of these parameters, the SED temperature; however, caution must be taken in comparing temperatures derived in different formalisms. In general, $T_{\rm d} > T_{\rm peak}$ as discussed by Casey (2012).

Due to the increasing temperature of the CMB at very high redshifts, the effect of (*a*) an increased dust temperature due to heating by CMB photons and (*b*) the reduced contrast of FIR observations when viewed against an increased CMB background, must be taken into account. We refer the reader to da Cunha et al. (2013) and Ota et al. (2014) for detailed overviews of these effects and how to correct for them. In addition, some studies (particularly at $z = 3$–5) use empirically derived SEDs in the FIR or fit low-redshift dusty galaxy templates to the observations (e.g., Álvarez-Márquez et al. 2019). The dust mass can be constrained from the Rayleigh–Jeans tail of the IR SED, at high wavelength beyond the peak and where the emission is expected to be optically thin. Here, the observed flux depends on the mass of dust, the dust mass absorption coefficient, and the luminosity distance ($d_{\rm L}$) as

$$S(\nu, T) = \frac{\kappa_\nu M_{\rm d}(B_\nu(T_{\rm d}) - B_\nu(T_{\rm CMB}))}{d_{\rm L}^2}. \qquad 4.$$

The dust mass is very sensitive to the assumed dust temperature with $M_{\rm d} \propto L_{\rm IR}\, T_{\rm d}^{-(4+\beta_{\rm d})}$. The dust mass absorption coefficient can vary in the range $5 < \kappa_0 < 30$ cm^2 g^{-1} (Hirashita et al. 2014), with a frequency dependence given by $\kappa_\nu = \kappa_0(\nu/\nu_0)^{\beta_{\rm d}}$ where the reference frequency corresponds to $\lambda_0 = 158\,\mu$m. We take $\kappa_0 = 8.94\,{\rm cm^2\,g^{-1}}$ as appropriate for dust ejected by a supernova (e.g., following Schouws et al. 2022). There has been considerable discussion about the dust temperature and, more recently, the $\beta_{\rm d}$ emissivity parameter in recent years, thanks to the combination of multiple bands with ALMA constraining the long wavelength decline and peak of the SED. We discuss the observed parameters in Section 5.

2.3. Interferometry

In interferometric observations the signals received by different antennas are correlated and recorded in the so-called UV-plane or Fourier space, with the complex visibilities consisting of an amplitude (providing flux information) and a phase (providing positional information). Each individual baseline between antennas has a resolution related to the baseline length, B: $\theta \sim \lambda/B$ (while larger structures are resolved out).

The ALMA large array consisting of 12-m-diameter antennas (i.e., the 12-m array) typically carries out observations with 40–50 antennas, dividing the effective collecting area over ~1,000 baselines. ALMA is designed with different configurations that are able to perform unresolved detection experiments of high-redshift galaxies as well as resolved observations. In **Figure 4**, we simulate a high-redshift source in the image plane and UV-plane to illustrate these different observations. The signal in the UV-plane is not affected by a point spread function (PSF)

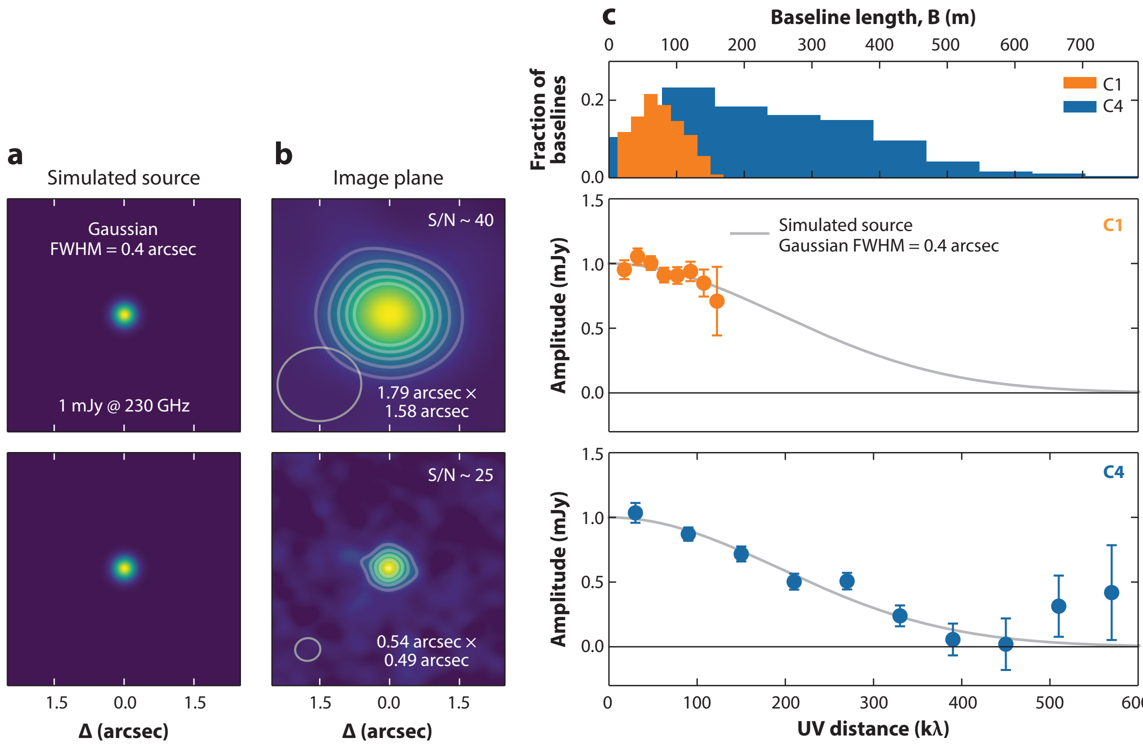

Figure 4

(*a*) Simulated Gaussian source with $R_e \sim 1$ kpc at $z \sim 7$ (FWHM = 0.4 arcsec) at 230 GHz. (*b*) We use two configurations (C1 and C4; synthesized beams of ~1.7 arcsec and ~0.5 arcsec, respectively) to simulate the observations in the image plane, at fixed rms/beam. The peak S/N reaches 40 for C1 and goes down by ~40% for C4. White contours are drawn at 5, 10, 15, 20, and 25σ, and the beam size is indicated as a gray ellipse in the bottom left corner of each panel. (*c*) The changing S/N can most easily be understood by comparing the baseline distance distribution of each configuration with the size of the source in the UV-plane. Gray lines show the intrinsic signal, and colored points show the binned mock observations, whereas the top panel shows the fraction of baselines as a function of baseline length. Abbreviations: FWHM, full width at half maximum; S/N, signal-to-noise ratio; UV ultraviolet.

(see **Figure 4*a***); however, with the Fourier transform to the image plane, the PSF or beam emerges from the finite sampling of the UV-plane by the baseline distribution (see **Figure 4*b***). The detection experiment (*upper panels* of **Figure 4**) with $\theta_{\rm beam} > 2 \times \theta_{\rm source}$ uses all baselines near the maximum amplitude of the source in the UV-plane, while the experiment with modest structural information (*bottom panels* of **Figure 4**), with $\theta_{\rm beam} \sim \theta_{\rm source}$, divides its baselines over the full source structure in the UV-plane, at the cost of signal-to-noise (S/N). The **Supplemental Text** provides additional information on UV-plane modeling, ALMA configurations, the imaging process, and observing strategies for high-redshift sources with ALMA.

LBGs: Lyman-break galaxies

LAEs: Lyman-α emitters

Supplemental Material >

3. SAMPLE OF ALMA-OBSERVED z > 6.5 SOURCES

In this section, we present a compilation of the ALMA follow-up of $z > 6.5$ galaxies and quasars to date. These 154 sources are then taken as the basis for the rest of the review, in which we provide consistent computations of the IR luminosity and obscured SFRs.

3.1. Sample Selection

The majority of known $z > 6.5$ galaxies and quasars have been selected based on their rest-frame UV emission, which probes the unobscured light from young stars. For reionization-era sources, the rest-UV is redshifted into the NIR filters of telescopes like the *Hubble Space Telescope* (HST) and now JWST in space, as well as NIR capable ground-based facilities like Visible and Infrared Survey Telescope for Astronomy (VISTA) and United Kingdom Infrared Telescope (UKIRT). Once detected in the NIR, high-redshift galaxy and quasar candidates are separated from the more numerous interloper populations (consisting of mainly red $z \simeq 1$–3 galaxies and ultracool brown dwarfs) through the Lyman-break technique. Here, the key spectral features are the blue rest-frame UV slope dominated by young stellar populations (parameterized as $\beta_{\rm UV}$, with $F_\lambda \propto \lambda^{\beta_{\rm UV}}$), and the strong Lyman-$\alpha$ break at 1216 Å resulting from absorption by the predominantly neutral IGM at these redshifts. Lyman-break galaxies (LBGs) that are typically selected from deep field programs show SFRs on the order of 1 to 100 $\rm M_\odot\,year^{-1}$, blue colors ($\beta_{\rm UV} \simeq -2$), and stellar masses on the order of $\log_{10}(M_\star/{\rm M_\odot}) = 8$–10 (see the review by Stark 2016). An additional class of sources is given by Lyman-α emitters (LAEs) (see Ouchi et al. 2020 for a review), of which large samples have been selected using narrow-band photometric filters. Here, a photometric excess in a narrow ($\lambda_{\rm obs} < 100$ Å) band in comparison to an encompassing broadband signals a strong emission line, wherein a source with rest-frame equivalent width of $EW_0 > 20$ Å is typically defined as an LAE. LAEs are shown to have lower dust attenuation and stellar masses, but higher sSFR, than LBGs at the same redshift and rest-frame UV luminosity (see the review by Ouchi et al. 2020). High-redshift candidate quasars, LBGs, and LAEs once selected are typically followed up with spectroscopic instruments (e.g., in the rest-UV or optical with JWST or ground-based facilities, or FIR with ALMA) to confirm the redshift through emission lines. Small samples of sources have been selected based on their FIR emission, but these have exclusively been serendipitous sources found within the ALMA observations of LBGs or quasars (e.g., Fudamoto et al. 2021, Wang et al. 2024a).

3.2. Deep Field Programs

ALMA has targeted deep extragalactic fields to provide millimeter/submillimeter constraints in combination with a wealth of auxiliary data from UV to radio telescopes. The first deep fields were performed in the Hubble Ultra Deep Field (UDF) as part of the pilot ALMA SPECtroscopic Survey (ASPECS) in the Hubble UDF (Walter et al. 2016) and "ALMA UDF" (Dunlop et al. 2017) programs, followed in Cycle 4 by the full ASPECS survey (Decarli et al. 2020).

These programs aimed to utilize the previous observations in this field to determine the line and continuum emission from galaxies over a broad range of redshifts. These programs identified no individual $z > 6$ detections, likely due to a combination of the strong dependence of obscured SFR on stellar mass (e.g., Bouwens et al. 2016, Dunlop et al. 2017), the flattening of the millimeter counts to low luminosity (González-López et al. 2020) and the SFR–$L_{[CII]}$ dependence (see Section 4.2). The highest-redshift object with a spectroscopic redshift detected in the dust continuum in ASPECS is $z = 3.711$ (Bouwens et al. 2020) and in the Hubble UDF $z = 5.00$ of Dunlop et al. (2017). In addition to blank field mosaics, foreground clusters have been targeted that allow strong gravitational lensing to be exploited in the search for faint high-redshift galaxies. The ALMA Lensing Cluster Survey (ALCS) (e.g., Fujimoto et al. 2023) targeted 33 lensing clusters. The highest-redshift source found in the ALCS with an ALMA detection was the multiply imaged $z = 6.07$ galaxy (Fujimoto et al. 2021), Cosmic Grapes. In addition, the Deep UNCOVER-ALMA Legacy High-Z (DUALZ) (Fujimoto et al. 2025) targeted the Abell 2744 cluster with Cycle 9 data and detected (with the prior on the redshift) a source at $z =$ 6.32. Other programs such as Mapping Obscuration to Reionization with ALMA (MORA) and Hubble Frontier Fields (HFF)-ALMA are too shallow to provide strong constraints on the line or continuum properties of individual known $z > 6.5$ galaxies in the field. For these deep field programs, it is only possible to provide stacked constraints on the dust continuum properties and upper limits on the prevalence of line emission. We show these constraints where relevant.

3.3. Targeted Programs

Numerous ALMA programs have targeted single or small (<10) samples of high-redshift sources for follow-up. The early observational programs tended to target first the [CII] line, with the dust continuum constraints coming essentially "for free" (e.g., Ota et al. 2014, Schaerer et al. 2015). The first programs were unsuccessful in finding [CII] or dust continuum, likely as they were targeting LAEs that appear to have a lower dust content and potential [CII] deficit. Follow-up of luminous LBGs were more successful in detecting the dust continuum (Bowler et al. 2018, 2022; Schouws et al. 2022), with several sources further detected in multiple bands (Knudsen et al. 2017, Hashimoto et al. 2019). These programs paved the way for several important ALMA large programs that have substantially increased the understanding of the FIR properties of $z > 6.5$ sources. The ALMA-REBELS large program (Cycle 7) (Bouwens et al. 2022) performed follow-up of a sample of 40 luminous $z > 6.5$ LBGs. It complemented the deep field programs by targeting the rare, higher-mass galaxy population. Another significant ALMA large program was A SPectroscopic Survey of Biased Halos In the Reionization Era (ASPIRE) (Wang et al. 2024b). ASPIRE targeted 25 $z \sim 7$ quasars to form a view of high-redshift galaxy properties, through measurements of the quasar host galaxy [CII] and dust emission. We also mention here ALMA Large Program to INvestigate [CII] at Early times (ALPINE) (Le Fèvre et al. 2020), a program that focused on $z = 4.5$–6 galaxies selected from the spectroscopically confirmed sample over the Cosmic Evolution Survey (COSMOS) field. ALPINE provides a key reference for higher-redshift samples; however, it is important to note that the selection function is different for many $z > 6.5$ samples as a spectroscopic redshift was required prior to observing with ALMA. Other relevant programs at $z < 6.5$ are Systematic Exploration in the Reionization Epoch using Nebular And Dust Emission (SERENADE), which targeted extremely UV-bright galaxies found within wide fields (Mitsuhashi et al. 2024), and [CII] Resolved ISM in STar-forming galaxies with ALma (CRISTAL), which was a large program following up the ~20 most massive and star-forming [CII] detected sources from ALPINE for high-redshift [CII] and dust continuum measurements (Herrera-Camus et al. 2025).

3.4. Compilation of a Catalog from the Literature

In this review, we aim to compile the published observations of $z > 6.5$ galaxies and quasars taken by ALMA and NOEMA since these telescopes first started taking data just over a decade ago. As introduced in Section 3.1, the known samples of high-redshift galaxies fall into several distinct categories, namely sources studied through deep mosaics (e.g., ALMA-UDF, ASPECS) that covered established extragalactic fields in addition to targeted follow-up of particular galaxy populations (LAEs, LBGs, quasars, lensed LBGs, etc.). At the time of publication of this review, the number of sources in our compilation is 154.[2] We assume a ΛCDM cosmology with $\Omega_M = 0.3$ and $\Omega_\Lambda = 0.7$, and $H_0 = 70\,\mathrm{km\,s^{-1}\,Mpc^{-1}}$ and a Chabrier (2003) initial mass function (IMF). We provide more notes on the catalog creation in the **Supplemental Text**.

Supplemental Material >

In this review, we recompute the L_{IR} for the full sample of galaxies using an assumed FIR SED with a gently evolving T_{d} according to the Sommovigo et al. (2022) relation, normalized at $z = 6.4$ to $T_{\mathrm{d}} = 41$ K (to match that derived by Mitsuhashi et al. 2024). We fix the emissivity to $\beta_{\mathrm{d}} = 1.8$, following the results of Witstok et al. (2023). In Section 5.4, we show a summary of the best-fit dust temperatures from a compilation of works at high redshift to justify this choice. FIR line luminosities were taken directly from the relevant publication, as these are not strongly model dependent. The other properties (e.g., rest-frame UV luminosity, stellar mass) are also included directly from the literature. The M_{UV} is uncorrected for dust attenuation. The rest-frame UV slope β_{UV} is also taken from the individual studies; however, we note that biases can arise from the measurement method (SED versus color derived, for example) (Faisst et al. 2020b).

An overview of the sample is shown in **Figure 5**, in which we show L_{IR}, M_{UV}, $L_{\mathrm{[CII]}}$, and $L_{\mathrm{[OIII]}}$ as functions of redshift (see also **Supplemental Table 1**). In the past few years, the redshift record for the detection of [OIII] has been pushed to the frontier, with several sources now confirmed by ALMA at $z = 11$–14.179 (Zavala et al. 2024, Schouws et al. 2025). The majority of published observations of galaxies with measurements of the FIR continuum are upper limits. The two highest-redshift detections of the continuum in a spectroscopically confirmed galaxy are MACS0416_Y1, at $z = 8.31$, followed by REBELS-18, at $z = 7.675$ (Inami et al. 2022), whereas there are several other higher-redshift detections in galaxies with photometric redshifts (REBELS-04, REBELS-37). J0313–1806 is the highest-redshift quasar with a continuum detection (Wang et al. 2024b).

4. LINE EMISSION

A wide range of lines emerging from molecular, neutral, and ionized gas are in principle accessible to ALMA at $z > 6.5$ (see **Figure 3**). Some of the basic parameters of these molecular, atomic, and ionic species and their line transitions are listed in **Table 1**. The primary challenge of detecting $z > 6.5$ galaxies with ALMA is the observed faintness of these distant systems.

4.1. Line Scanning and the Spectroscopic Redshift Frontier

Due to the combination of their inherent brightness and visibility in the high-transmission ALMA bands at $z > 6.5$ (see **Supplemental Text**), [CII] λ158 μm and [OIII] λ88 μm (particularly visible above $z \gtrsim 8.3$) (Bouwens et al. 2022) have been the most targeted emission lines in EoR galaxies. The earliest attempts at detecting these lines were sources with confident spectroscopic redshift from bright Lyman-α emission—the only bright spectral line accessible from the ground with optical and NIR detectors. Although some of these observations were successful out to

[2] For the most up-to-date compilation, see **https://github.com/raabowler/hzalmacat/tree/main**.

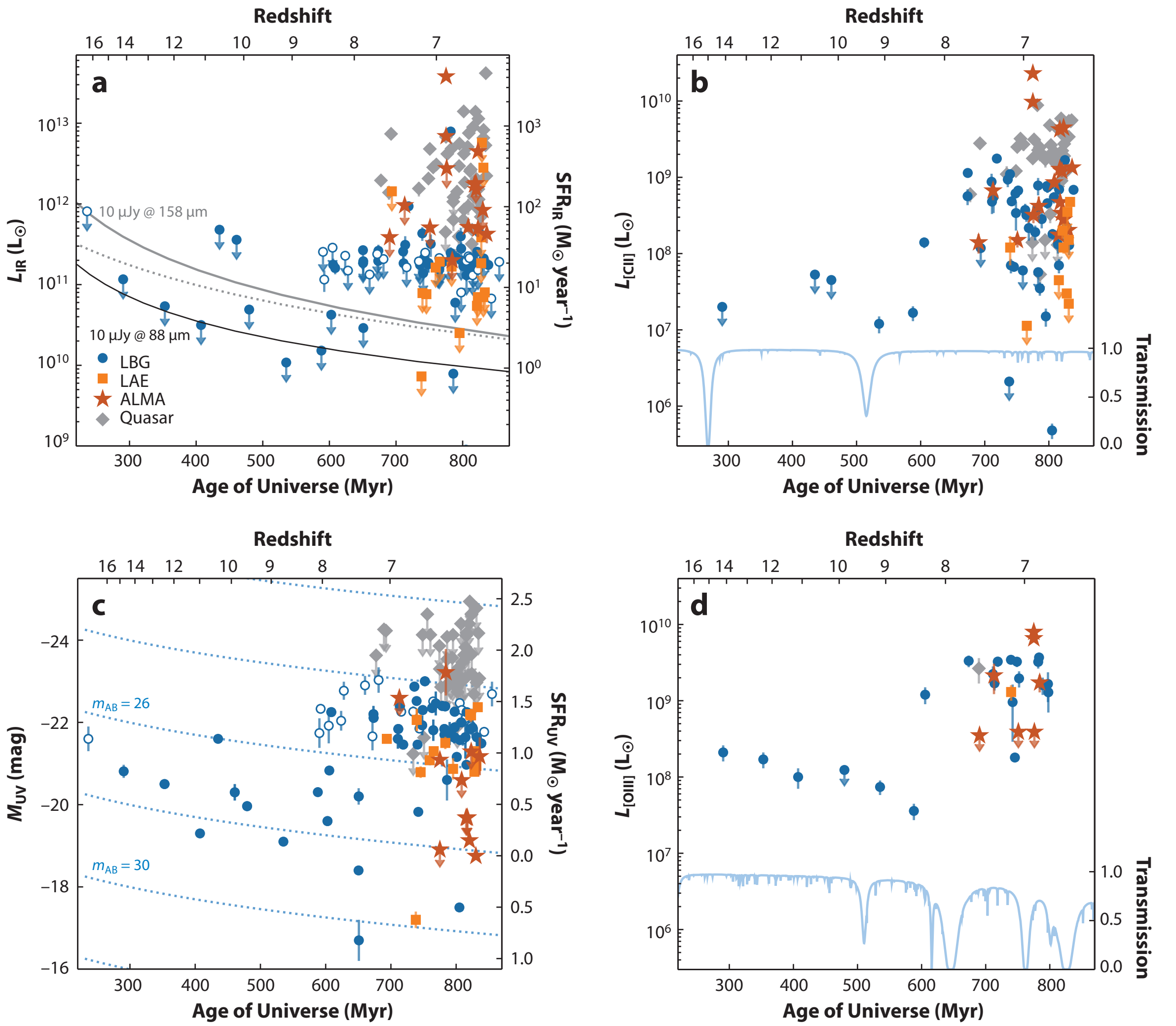

Figure 5

An overview of the luminosities of the sample of $z > 6.5$ sources observed with ALMA and NOEMA as a function of Universe age. We show the derived infrared luminosity (*a*); the measured $L_{[CII]}$ (*b*) and $L_{[OIII]}$ (*d*), respectively (with the atmosphere transmission on the right-hand axis); and the absolute UV magnitude (*c*). For panels *a* and *c*, we also show a conversion to SFR on the right-hand axis. For the quasars, we estimate the galaxy M_{UV} as 10% of the observed quasar M_{UV} and show this as an upper limit. In both plots, the open symbols illustrate photometric redshifts, whereas filled symbols are spectroscopic (from either far-IR or UV/optical emission lines). Upper limits are given as 3σ. Abbreviations: ALMA, Atacama Large Millimeter/submillimeter Array; LAE, Lyman-α emitter; LBG, Lyman-break galaxy; NOEMA, NOrthern Extended Millimeter Array; SFR, star-formation rate.

$z = 7.21$ (Inoue et al. 2016, Knudsen et al. 2016, Pentericci et al. 2016, Bradač et al. 2017), the number of LAEs significantly declines beyond $z \sim 6.5$ (Ouchi et al. 2020), owing to the scattering of Lyman-α photons when encountering HI in the IGM. Indeed, one of the hopes for the high-redshift community when ALMA first came online was that of being a "redshift machine": scanning for bright lines by designing multiple ALMA setups with contiguous frequency coverage as a way of obtaining spectroscopic confirmation of galaxies. However, the initial faintness of [CII] in LAE galaxies (Ouchi et al. 2013, Maiolino et al. 2015, Knudsen et al. 2016) and a few unsuccessful line scans for [CII] (González-López et al. 2014, Schaerer et al. 2015, Knudsen et al. 2017)—some with the significantly less sensitive PdBI (predecessor of NOEMA)—discouraged many further ALMA line-scanning experiments.

PDRs: photodissociation regions

Smit et al. (2018) obtained the first ALMA spectroscopic confirmation of LBGs in the EoR without Lyman-α redshifts by targeting [CII] in galaxies that had additional photometric redshift constraints from the *Spitzer Space Telescope*. Two more pilot studies with NOEMA and ALMA confirmed the utility of [CII] as an alternative to Lyman-α (Molyneux et al. 2022, Schouws et al. 2023), with in particular UV-bright galaxies showing [CII]-luminous line emission. A few studies have suggested that both UV luminosity and the absence of Lyman-α—which is more common in low-mass, metal-poor galaxies with low dust content—are important empirical indicators for [CII] visibility (e.g., Matthee et al. 2019, Harikane et al. 2020). Following on from these initial pilots, the first ALMA large program was approved to significantly increase the number of spectroscopically confirmed UV-bright galaxies in the EoR (REBELS) (Bouwens et al. 2022).

Beyond $z > 8$, two high-profile spectroscopic confirmations targeting [OIII] followed the initial [CII] line-scanning results. The [OIII] detection in a lensed galaxy at $z = 9.1$ by Hashimoto et al. (2018) held the record for the most distant spectroscopic line confirmation until the commissioning of JWST. Not long thereafter, Tamura et al. (2019) spectroscopically confirmed another brightly lensed galaxy at $z = 8.3$ through [OIII] line scanning. Until recently, the lack of bright (lensed) galaxy candidates beyond $z > 8$ has limited the progress of line scanning at the redshift frontier (van Leeuwen et al. 2025).

With the groundbreaking datasets of JWST, new opportunities for ALMA as a redshift machine have emerged. Although Near Infrared Spectrograph (NIRSpec) can observe rest-frame optical lines such as [OIII] λ5007 Å out to $z \sim 9.4$, few bright lines are accessible to NIRSpec for galaxy candidates (selected with Near Infrared Camera or NIRCam) above $z > 10$, with spectroscopic observations relying instead on the continuum break at the wavelength of Lyman-α for confirmation (e.g., Curtis-Lake et al. 2023). Although some of the first attempts at line scanning on targets $z > 10$ have been unsuccessful (Harikane et al. 2022, Bakx et al. 2023, Fujimoto et al. 2023, Kaasinen et al. 2023, Popping 2023, Yoon et al. 2023), recent results suggest these observations did not have the required depth to detect a line (Zavala et al. 2024). Indeed, the first successful [OIII] line scan above $z > 10$ revealed a precision redshift of $z = 14.179$ for a galaxy previously estimated to be at $z \sim 14.3$ based on NIRSpec continuum break information (Carniani et al. 2024, Schouws et al. 2025). This major ALMA success suggests the future redshift frontier will require the synergy of JWST and ALMA spectroscopy, such that NIRSpec can provide a tight prior on the redshift from continuum observations, whereas ALMA provides precision redshift information from deep integrations over a small redshift range (requiring only a few frequency setups for a spectral line scan).

4.2. [CII] λ158-μm Emission

Carbon has a first ionization potential (11.3 eV) below that of hydrogen and, therefore, far-ultraviolet (FUV) photons (6–13.6 eV) that permeate the galaxy ionize carbon in all but the most dense, self-shielded clouds. As a result, [CII] λ158 μm traces ionized, neutral, and even molecular gas, including warm, dense photodissociation regions (PDRs), the cold neutral medium, and diffuse ionized medium (e.g., Pineda et al. 2013). As a multimedium tracer, the usefulness of [CII] as a diagnostic tool for ISM conditions has been debated (e.g., Casey et al. 2014); however, its use as a kinematic tracer of the ISM has been widely recognized (see Section 6.2).

Dedicated observing programs have found evidence for neutral/molecular gas as the dominant emission for [CII] λ158 μm in $z > 6.5$ galaxies (see Section 4.4.2). This is consistent with emission line analyses from JWST, which find high ionization parameters (high [OIII]/[OII]) are common in $z > 6.5$ galaxies, suggesting the ionization structure within HII regions is weighted toward highly ionized species, and carbon could be doubly or even triply ionized within these regions (e.g., Cameron et al. 2023).

These findings potentially justify the use of [CII] as a tracer of the gas mass in distant galaxies. As traditional gas mass tracers such as CO are too faint to detect for all but the most extreme starburst galaxies at $z > 6.5$, [CII] is the only cool/cold gas tracer that is observationally accessible. We review the empirical relations and proposed calibrations for [CII] with respect to the SFR and to molecular and neutral gas mass.

4.2.1. $L_{[CII]}$–SFR relation. In the local Universe, the relation between $L_{[CII]}$ and SFR has been investigated in galaxies with a wide range of metallicities, SFRs, active galactic nucleus (AGN) contribution, and ISM conditions. In particular, De Looze et al. (2014) derive the following relation based on a large compilation of $z \sim 0$ dwarf galaxies (in particular from the Dwarf Galaxy Survey or DGS) (Madden et al. 2013), AGNs, and FIR-bright galaxies out to $z > 0.5$:[3]

$$\log \mathrm{SFR}/\mathrm{M}_\odot\,\mathrm{year}^{-1} = (-6.99 \pm 0.14) + (1.01 \pm 0.02) \times \log L_{[CII]}/\mathrm{L}_\odot, \qquad 5.$$

with 0.42 dex scatter. Either the origin for this relation could be the importance of FUV radiation from young stars in heating PDRs (see **Supplemental Text**), whose cooling is dominated by [CII] emission, or else [CII] λ158 μm could be an important tracer of molecular gas (see Section 4.2.2) and the $L_{[CII]}$–SFR relation is a manifestation of the integrated Kennicutt–Schmidt relation (Kennicutt & Evans 2012, De Looze et al. 2014). In **Figure 6**, we show the $z > 6.5$ compilation with respect to this relation and find good agreement within the 1σ scatter over ~3 dex in SFR, which is consistent with findings from ALPINE at $z \sim 4$–6 (Schaerer et al. 2020), possibly suggesting the Kennicutt–Schmidt relation could hold out to the EoR.

Supplemental Material >

At low SFRs, galaxies might have a mild bias toward low $L_{[CII]}$/SFR ratios. This is consistent with local metal-poor dwarf galaxies from the DGS, where lower SFR galaxies are typically lower metallicity (12 + [O/H] < 8.0, $Z < 0.2\,\mathrm{Z}_\odot$) and have lower obscuration fractions ($\mathrm{SFR_{UV}} > \mathrm{SFR_{IR}}$). This is furthermore consistent with simulations by Vallini et al. (2015) that predict a systematic offset of the $L_{[CII]}$–SFR relation for metal-poor galaxies (see **Figure 6** for $Z = 0.05\,\mathrm{Z}_\odot$). Other empirical indicators of low $L_{[CII]}$/SFR in the DGS are a high ionization parameter or burstiness (Algera et al. 2025; see also Section 4.3.3); a high dust temperature (see also Bakx et al. 2020); a large volume filling factor of ionized gas; and hot, dense neutral/PDR gas (De Looze et al. 2014).

At low and intermediate redshifts, ULIRGs and DSFGs also have a well-known [CII] deficit (Casey et al. 2014, Hodge & da Cunha 2020, Decarli & Díaz-Santos 2025). However, this effect is not clearly present in the compilation of $z > 6.5$ galaxies at the high-SFR end of the $L_{[CII]}$–SFR relation.

4.2.2. $L_{[CII]}$–M_{H_2} relation. Molecular gas is the fuel for star formation and, given the faintness of low-J CO lines, [CII] is the only feasible tracer of cold gas in larger samples at high redshift. In recent years, an increasing body of literature has aimed to understand the correlation between $L_{[CII]}$ and M_{H_2}. Zanella et al. (2018) provided the most commonly used calibration of [CII] λ158 μm as a molecular gas tracer from a sample of MS galaxies at $z \sim 2$ and an additional

[3]Including starbursts (SBs; massive galaxies with star-formation-powered FIR radiation), ultraluminous infrared galaxies (ULIRGs; $L_{IR} > 10^{12}\,\mathrm{L}_\odot$), and dusty star-forming galaxies (DSFGs; rest-frame MIR- or FIR-selected high-redshift galaxies).

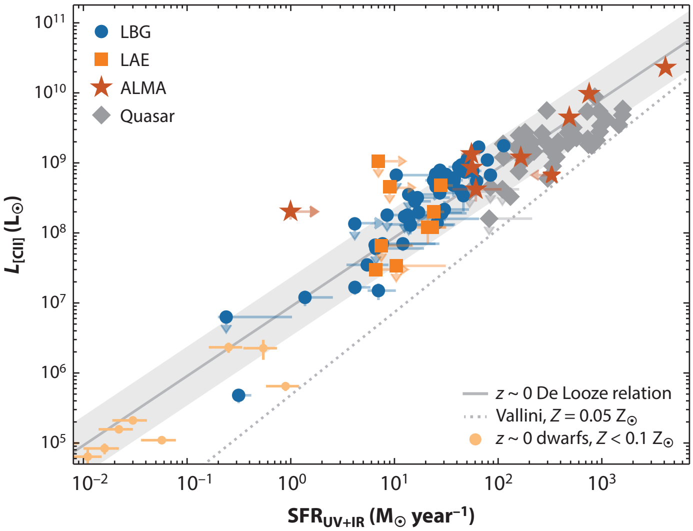

Figure 6

The relation between SFR and $L_{[CII]}$ for the $z > 6.5$ literature compilation, compared to the local relation and scatter measured by De Looze et al. (2014) (*gray line* and *gray shaded region*). Very metal-poor galaxies ($Z < 0.1\,Z_\odot$) at $z \sim 0$ are shown in yellow, whereas the simulated Vallini et al. (2015) relation for $Z = 0.05\,Z_\odot$ galaxies is shown as a dotted line. Upper error bars on the SFR include 1σ limits on dust continuum nondetections. Abbreviations: ALMA, Atacama Large Millimeter/submillimeter Array; LAE, Lyman-α emitter; LBG, Lyman-break galaxy; SFR, star-formation rate.

literature sample from $z \sim 0$ to $z \sim 5$. They define the [CII]-to-H_2 conversion factor as

$$\alpha_{[CII]}(M_\odot/L_\odot) = M_{H_2}/L_{[CII]}, \quad 6.$$

which is an analogy to the widely used CO-to-H_2 conversion factor, α_{CO}. Good agreement with this conversion was found by Dessauges-Zavadsky et al. (2020) and Aravena et al. (2024) using low angular resolution dynamical constraints from LBGs in ALPINE ($z \sim 4$–6) and REBELS ($z = 6$–8), respectively. Rowland et al. (2024) further confirm the latter with high-resolution dynamical measurement in REBELS-25.

Furthermore, various studies have found strong correlations between [CII] λ158 μm and CO(1–0) at low to intermediate redshifts (e.g., Gullberg et al. 2015, Zhao et al. 2024), supporting the use of [CII] λ158 μm as a molecular gas tracer; however, the uncertainty in the α_{CO} factor remains one of the main systemic uncertainties behind the derived variation in $\alpha_{[CII]}$. Zhao et al. (2024) derive $\alpha_{[CII]} = 8.12 \times \alpha_{CO}$ and $\alpha_{[CII]} = 34.9\,M_\odot/L_\odot$, assuming $\alpha_{CO} = 4.3\,M_\odot\,(\mathrm{K\,km\,s^{-1}\,pc^2})^{-1}$, which is in good agreement with Zanella et al. (2018). Studies of ULIRGs, SMGs (submillimeter galaxies), and QSOs (quasi-stellar objects) have typically found much lower values for $\alpha_{[CII]}$; e.g., Swinbank et al. (2012) and Kaasinen et al. (2024) find 10 and 5 $M_\odot/L_\odot$, assuming an α_{CO} of 1 and 0.8 $M_\odot\,(\mathrm{K\,km\,s^{-1}\,pc^2})^{-1}$, respectively. These lower values for L_{IR}-bright systems are confirmed with dynamical studies by Gullberg et al. (2018) and Rizzo et al. (2021), suggesting systemic changes in $\alpha_{[CII]}$ with stellar mass, dust fraction, and/or metallicity. A compilation of conversion factors from the literature is presented in **Table 2**.

SMGs: submillimeter galaxies

QSOs: quasi-stellar objects

Furthermore, in local metal-poor galaxies, CO(1–0) has been suggested to be a poor tracer of the molecular reservoir owing to a great fraction of CO-dark molecular gas, where reduced dust shielding at lower metallicity dissociates CO in all but the densest molecular cores. Madden et al. (2020) show that CO-dark molecular regions are well traced by [CII] λ158 μm and derive

Table 2 [CII]-to-H$_2$ conversion factor

$\alpha^{a}_{[CII]}$ ($M_\odot/L_\odot$)	Reference(s)	Redshift	Target selection	Notes
31	Zanella et al. 2018	$z \sim 2$	MS galaxies	M_{H_2} from M_{dust}
	Dessauges-Zavadsky et al. 2020	$z \sim 4{-}6$	LBGs	M_{H_2} from M_{dyn}
	Aravena et al. 2024, Rowland et al. 2024	$z \sim 6{-}8$	LBGs	M_{H_2} from M_{dyn}
34.9	Zhao et al. 2024	$z \sim 0^{b}$	MS galaxies, ETGs, LIRGs[c], ULIRGs, LBAs[d], DSFGs	M_{H_2} from CO ($\alpha_{CO} = 4.3$)
81	Madden et al. 2020	$z \sim 0$	Metal-poor dwarfs	Modeling CO-dark gas
48	Ramambason et al. 2024	$z \sim 0$	Metal-poor dwarfs	Modeling CO-dark gas
10	Swinbank et al. 2012	$z \sim 2{-}4$	ULIRGs, QSOs	M_{H_2} from CO ($\alpha_{CO} = 1$)
	Gullberg et al. 2018	$z \sim 4.5$	SMGs	M_{H_2} from M_{dust}
7	Rizzo et al. 2021	$z \sim 4{-}5$	DSFG	M_{H_2} from M_{dyn}
5	Kaasinen et al. 2024	$z \sim 6.5{-}7$	QSOs	M_{H_2} from CO ($\alpha_{CO} = 0.8$)

[a]$M_{mol}/M_\odot = \alpha_{[CII]} \times L_{[CII]}/L_\odot$.
[b]The $z \sim 0$ sample is complemented by a small sample of high-redshift DSFGs out to $z \sim 6$.
[c]$L_{IR} > 10^{11}$ $L_\odot$.
[d]Local galaxies are matched to LBGs in surface brightness and color.
Abbreviations: DSFG, dusty star-forming galaxy; ETG, early-type galaxy; LBA, Lyman-break analog; LBG, Lyman-break galaxy; LIRG, luminous infrared galaxy; MS, main sequence; QSO, quasi-stellar object; SMG, submillimeter galaxy; ULIRGs, ultraluminous infrared galaxy.

$M_{H_2} = 10^{2.12} \times [L_{[CII]}]^{0.97}$, which corresponds with $\alpha_{[CII]} = 76{-}87\,M_\odot/L_\odot$. Ramambason et al. (2024) revisit the CO-dark gas modeling using a more complex geometry of the PDR and find $\alpha_{[CII]} = 43{-}52\,M_\odot/L_\odot$.

In summary, a new picture is emerging in which [CII] λ158 μm is a good tracer of gas mass, although with modest variations for different galaxy samples. Aravena et al. (2024) study the molecular gas in the REBELS sample ($z = 6{-}8$) with the Zanella et al. (2018) conversion and find the median molecular gas-to-stellar mass ratios and molecular gas-depletion timescales are roughly constant with redshift over the range of $z = 2{-}7$, whereas the cosmic density of molecular gas at $z \sim 7$ continues a steep decline from $z \sim 2$.

4.2.3. $L_{[CII]}$–M_{HI} relation. In the optically thin limit, and assuming only collisional excitation, the [CII] λ158 μm luminosity and the gas mass can theoretically be directly related for a given gas density and temperature (e.g., Hailey-Dunsheath et al. 2010, Veilleux et al. 2020, Herrera-Camus et al. 2021, Litke et al. 2022):

$$\frac{M_H}{M_\odot} = f_{[CII],neutral} \cdot 0.77 \left(\frac{1.4 \times 10^{-4}}{X(C^+)}\right) \left[\frac{1 + 2e^{-91.25/T} + n_{crit}/n}{2e^{-91.25/T}}\right] \frac{L_{[CII]}}{L_\odot}, \qquad 7.$$

where $X(C^+)$ is the abundance of singly ionized carbon and $C^+/H = 1.4 \times 10^{-4}$ obtained from absorption spectroscopy in the Milky Way (Savage & Sembach 1996) is assumed. A common assumption is the maximal excitation case, where $n \gg n_{crit}$ and $T \gg 91$ K such that $M_H/M_\odot \sim f_{[CII],neutral} \cdot L_{[CII]}/L_\odot$ becomes a fairly conservative lower limit for the neutral gas mass traced by [CII] λ158 μm. For a wider range in ISM conditions, Herrera-Camus et al. (2021) tabulate values of κ_{HI}, where $M_H/M_\odot = \kappa_{[CII]} \cdot L_{[CII]}/L_\odot$.

Heintz et al. (2021) use damped Lyman-α (DLA) systems at $z \gtrsim 2$ to measure both the hydrogen and [CII*] 1335.7 Å column density and (assuming $M_{HI}/L_{[CII]} = N_{HI}/N_{[CII^*]} \times 1.165 \times 10^{-4}\,M_\odot/L_\odot$) derive a metallicity-dependent relation between [CII] λ158 μm luminosity and the neutral gas mass:

$$\log M_{\rm HI}/{\rm M}_\odot = (-0.87 \pm 0.09) \times \log Z/{\rm Z}_\odot + (1.48 \pm 0.12) + \log L_{\rm [CII]}/{\rm L}_\odot. \qquad 8.$$

At solar metallicity, this corresponds to $\kappa_{\rm HI} = 4.1$, which is somewhat above the maximal excitation assumption but broadly consistent with values reported by Herrera-Camus et al. (2021) for moderate gas density and temperatures ($T \sim 10^2$–10^3 K, $n \sim 10^3 {\rm cm}^{-3}$).

Using this calibration, Heintz et al. (2022) study the gas fractions of REBELS galaxies at $z \sim 7$ and find high gas fractions; $M_{\rm HI}/M_* \sim 10$ ($f_{\rm gas} \sim 90\%$). They furthermore argue that at these redshifts only ~10% of the cosmic HI gas content is confined in galaxies and associated with the star-forming ISM.

4.3. [OIII] λ88-μm Emission

Two times ionized oxygen requires a radiation field above 35.1 eV, which is typically generated by the hard stellar spectra of metal-poor stars in gas with high ionization parameters (high radiation intensity for a given particle density). Even before the launch of JWST, rest-frame optical [OIII] lines were inferred to be quite luminous in a significant fraction of the LBG population (e.g., Smit et al. 2014, 2015), and [OIII] λ88 μm observations with ALMA have been successful in nearly all targeted LBGs and LAEs in which a spectroscopic redshift was known and the line falls in a good transmission window of the atmosphere.

4.3.1. $L_{\rm [OIII]}$–SFR relation. In the local Universe, there are clear differences in the $L_{\rm [OIII]}$–SFR relation for different galaxy selections, with metal-poor dwarf galaxies following the relation in Equation 9,

$$\log {\rm SFR/M_\odot\,year^{-1}} = (-6.71 \pm 0.33) + (0.92 \pm 0.05) \times \log L_{\rm [OIII],dwarfs}/{\rm L}_\odot, \qquad 9.$$

with 0.30-dex scatter, whereas a broader sample of dwarf galaxies, AGNs, and FIR-bright galaxies follow this relation,

$$\log {\rm SFR/M_\odot\,year^{-1}} = (-6.71 \pm 0.33) + (0.92 \pm 0.05) \times \log L_{\rm [OIII],all}/{\rm L}_\odot, \qquad 10.$$

with a broad 0.66-dex scatter. **Figure 7** shows good agreement of $z > 6.5$ LBGs and LAEs with the local dwarf galaxy relation, as well as serendipitous ALMA-selected galaxies next to LBGs (Fudamoto et al. 2021), whereas IR-bright sources and quasars are broadly consistent with the general relation.

4.3.2. [OIII] λ88 μm as a metallicity indicator. In both metal-poor dwarf galaxies at $z \sim 0$ and high-redshift LAEs and LBGs, the high [OIII] λ88 μm/SFR ratios have proven challenging to model with photoionization codes (e.g., `Cloudy`). For a simple dust screen configuration, Harikane et al. (2020), Witstok et al. (2022), and Killi et al. (2023) find that solar metallicity, in combination with relatively low gas density ($\log n/{\rm cm}^{-3} = 0.5$–$2.0$) in the star-forming regions, is preferred. Although these high metallicities were already difficult to reconcile with the early epoch in which these sources are found (i.e., in the pre-JWST era), JWST oxygen abundance measurements are showing clear inconsistencies (e.g., Harikane et al. 2025, Scholtz et al. 2025, Usui et al. 2025).

In $z \sim 0$ dwarf galaxies, which have both high [OIII] λ88 μm/SFR and low-oxygen abundance ($z \lesssim 0.2\,{\rm Z}_\odot$), Cormier et al. (2015) propose a high filling factor of diffuse highly ionized gas (responsible for [OIII] λ88 μm/SFR) due to a low covering factor of the PDR, such that the star-forming regions start leaking ionizing photons that escape out to great distances. This is similar to the two-phase ionized gas models proposed by Harikane et al. (2025) and Usui et al. (2025) to explain the observed [OIII] λ88 μm/[OIII] λ5007 Å and [OIII] λ4363 Å/[OIII] λ5007 Å line ratios and discrepancies between optical- and IR-derived electron densities. Such a model

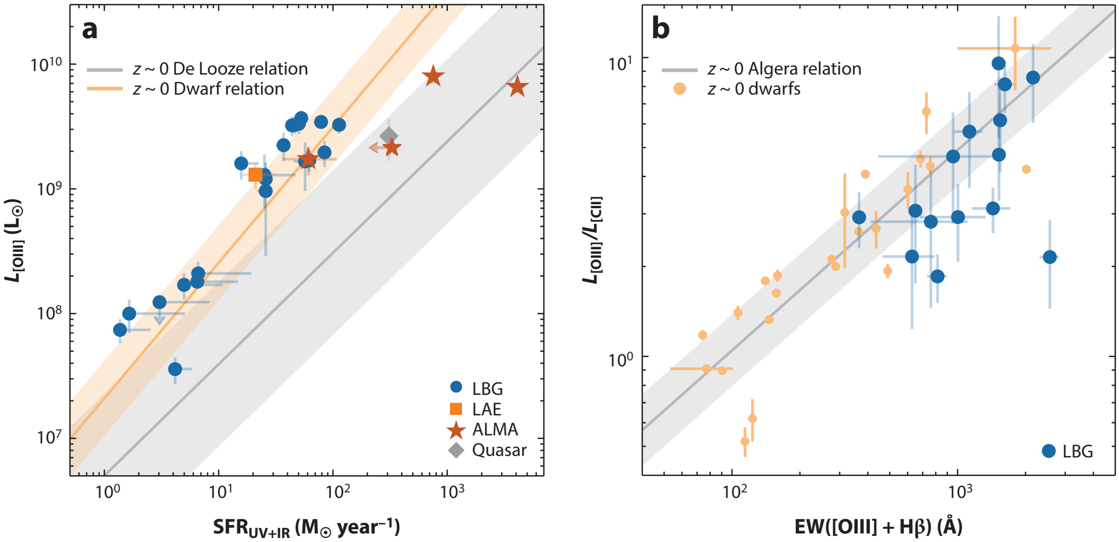

Figure 7

(*a*) The literature compilation of $z > 6.5$ sources with respect to the $z \sim 0$ scaling relations and scatter measured by De Looze et al. (2014) for metal-poor dwarfs (*orange line* and *orange shaded region*) and the full local galaxy sample (*gray line* and *gray shaded region*). (*b*) The far-IR $L_{[\mathrm{OIII}]}/L_{[\mathrm{CII}]}$ ratio as a function of the optical [OIII]+Hβ equivalent width, a common star-formation burstiness indicator, for $z \sim 0$ dwarf galaxies (*yellow points*), including the scaling relation and scatter measured by Algera et al. (2025; *gray line* and *shaded region*) and the $z > 6.5$ compilation. Abbreviations: EW, equivalent width; SFR, star-formation rate.

would also suggest that oxygen abundance measurements from JWST alone could be significantly underestimated (up to 0.8 dex) (Harikane et al. 2025).

Despite the challenges in interpreting [OIII] λ88 μm, it might be possible to use [OIII] λ88 μm/SFR as a rough metallicity tracer, using the empirical relation by Jones et al. (2020),

$$12 + \log(\mathrm{O}^{++}/\mathrm{H}^{+}) = 7.735 + \log \frac{L_{[\mathrm{OIII}]}}{10^7\,\mathrm{L}_\odot} - \log \frac{\mathrm{SFR}}{\mathrm{M}_\odot\,\mathrm{year}^{-1}}, \qquad 11.$$

and using an SFR derived from the Balmer lines and $T_e = 1.5 \times 10^4$ K and $n_e = 250\,\mathrm{cm}^{-3}$. Assuming $12 + \log(\mathrm{O/H}) \sim 0.17 + 12 + \log(\mathrm{O}^{++}/\mathrm{H}^{+})$ (i.e., an ionization correction factor of 0.17 dex), Jones et al. (2020) find good agreement for local metal-poor dwarfs between [OIII] λ88 μm/SFR and optical direct T_e oxygen abundance measurements (0.26-dex scatter).

Using [OIII] λ88 μm/SFR as a metallicity indicator, ALMA results have shown that galaxies above $z > 11$ are already enriched up to ~10–30% of the solar oxygen abundance (Zavala et al. 2024, Schouws et al. 2025, Witstok et al. 2026).

4.3.3. [OIII] λ88 μm/[CII] λ158 μm ratio. The line ratio of the two brightest lines accessible with ALMA at $z > 6.5$, [OIII] λ88 μm/[CII] λ158 μm, provides a rough indicator of the ISM conditions of a galaxy. Just as [OIII] λ88 μm/SFR ratios are systematically higher than for typical star-forming galaxies at $z \sim 0$ (Section 4.3.2), [OIII]/[CII] line ratios are some of the highest observed in the local Universe (e.g., Inoue et al. 2016, Carniani et al. 2020). Although [OIII] emission requires an ionizing radiation field above 35.1 eV, PDR-dominated [CII] emission relies on FUV radiation between 6 and 13.6 eV. A natural assumption is therefore that the burstiness of the recent SFH dominates the line ratio at a fixed C/O abundance. Indeed, $z \sim 0$ metal-poor dwarfs show a strong correlation with the equivalent width of optical emission lines, EW([OIII]+Hβ), which is often used as a proxy for star-formation burstiness (Witstok et al. 2022, Algera et al. 2025). **Figure 7** shows a compilation of $z > 6.5$ sources with both [OIII]/[CII] and EW([OIII]+Hβ) measurements with respect to the local relation, fitted by Algera et al. (2025) to the DGS sample:

$$\log\left(\frac{L_{[\mathrm{OIII}]}}{L_{[\mathrm{CII}]}}\right) = (0.69 \pm 0.07) + (0.67 \pm 0.11) \times \left(\log\left(\frac{\mathrm{EW}_{[\mathrm{OIII}]+\mathrm{H}\beta}}{\mathrm{\AA}}\right) - 3\right), \quad 12.$$

with 0.12 dex scatter. The agreement of our high-redshift compilation with the local metal-poor dwarf sample suggests similar physics drives the [OIII]/[CII] ratio across cosmic time.

Possibly linked to the burstiness of star formation, Harikane et al. (2020) find from `Cloudy` modeling of [OIII]/SFR as a function of [CII]/SFR that systematically higher ionization parameters are needed to explain the high [OIII]/[CII] ratios, possibly combined with lower PDR covering factors. Algera et al. (2025) perform the first study that uses JWST spectroscopy alongside [OIII]/[CII] to disentangle the influence of metallicity (12+log(O/H)), ionization parameter ([OIII] λ5007 Å/[OII] λ3727,29 Å; O_{32}) and burstiness (EW([OIII]+Hβ)) on high-redshift galaxies and $z \sim 0$ dwarf galaxies simultaneously. Although no significant correlation of [OIII]/[CII] with metallicity is found at high or low redshift, both ionization parameter and burstiness have statistically significant correlations with [OIII]/[CII] in the low-redshift dwarf sample, which is primarily driven by low [CII]/SFR at high EW([OIII]+Hβ) and O_{32}. However, comparing the high-redshift sample with the local relations, Algera et al. (2025) find high-redshift galaxies are significantly offset to higher [OIII]/[CII] at fixed O_{32}. This suggests that ionization parameter alone is not sufficient to explain the high [OIII]/[CII] ratios in high-redshift galaxies, and increased burstiness and/or lower covering factors of the PDR are also important drivers for explaining the observed properties.

4.4. Other Lines

Supplemental Material >

Although [CII] λ158 µm and [OIII] λ88 µm have been the workhorse lines of ALMA high-redshift observations owing to their inherent brightness, a range of fainter lines originating in the ionized, neutral, and molecular phases of the ISM can be observed or constrained with ALMA bands 1–10 as galaxies at increasing high redshift are discovered with JWST (see also the **Supplemental Text**).

4.4.1. [OIII] λ52 µm.

The fine-structure line of double ionized oxygen at the 52-µm line has been heralded as the ideal line to measure oxygen abundance and constrain electron density and temperature when combined with the [OIII] λ88 µm and [OIII] λ5007 Å lines (Jones et al. 2020). However, only a handful of detections and upper limits have been reported to date (Killi et al. 2023, Harikane et al. 2025) at redshift $z = 6.2{-}7.2$. This lack of data is mainly due to the high frequency of the line requiring band 9 observations in a relatively compact configuration to ensure the source remains unresolved (putting tight constraints on the observing schedule). Perhaps surprisingly, Killi et al. (2023) and Harikane et al. (2025) report relatively faint [OIII] λ52 µm lines with [OIII] λ52 µm/[OIII] λ88 µm < 1, suggesting modest electron density of the ionized gas ($n_e < 100\,\mathrm{cm}^{-3}$) in all but one galaxy. This is in contrast to the electron densities measured in the rest-frame optical with JWST spectroscopy, which suggests $n_e \sim 200{-}1{,}700\,\mathrm{cm}^{-3}$ (Harikane et al. 2025). This discrepancy provides increasing evidence for the presence of diffuse, warm, yet highly ionized gas surrounding hot, dense HII regions (see Section 4.3.2).

4.4.2. [NII] λ205 µm and [NII] λ122 µm.

The single ionized nitrogen ion has two fine-structure transitions that—if sufficiently bright—are easily accessible with ALMA in bands 6 and 7 at $z \sim 7$. Each transition provides different constraints on the ISM.

[NII] λ205 μm is most commonly used to understand the fraction of [CII] λ158 μm emitted by ionized and neutral (PDR) gas in the ISM. Nitrogen and carbon have similar second ionization potentials (29.6 and 24.4 eV, respectively), whereas the first ionization potential of nitrogen (14.5 eV) is slightly above that of hydrogen and traces exclusively ionized gas (in contrast to carbon; see Section 4.2). Furthermore, [NII] λ205 μm and [CII] λ158 μm have similar excitation energies and critical densities (∼45 cm^{-3}) when electrons are the collisional partners. As a result, the [NII] λ205 μm line emission scales directly with the ionized fraction of the [CII] λ158 μm emission ($L_{[NII]} \sim L_{[CII],ion}$), with their ratio only dependent on the gas phase C/N abundance. The [CII] λ158 μm/[NII] λ205 μm ratio is therefore used to disentangle the [CII] λ158 μm arising from different phases (ionized versus neutral gas) of the ISM. Witstok et al. (2022) reported the first nondetection of [NII] λ205 μm in an LBG at $z = 6.7$, suggesting the [CII] λ158 μm is arising predominantly from the neutral gas, despite the source having high [OIII] λ88 μm/[CII] λ158 μm that possibly indicates a high volume filling factor of (highly) ionized gas (Cormier et al. 2015). Deeper observations were taken on a sample of four [CII]-bright luminous LBGs at $z = 6$–7 by Fudamoto et al. (2025), confirming ∼74–96% of [CII] λ158 μm emission is PDR dominated. Deep upper limits on the [NII] λ205 μm line in a quasar host galaxy at $z = 7.5$ similarly suggest >75% of the [CII] emission is PDR dominated (Novak et al. 2019).

[NII] λ122 μm has a high critical density, and therefore the [NII] λ205 μm/[NII] λ122 μm line ratio constrains the electron density of the ionized gas for n_e between 10 and 3,000 cm^{-3} (e.g., Herrera-Camus et al. 2016). Furthermore, the [NII] λ122 μm/[OIII] λ88 μm line flux ratio constrains the ionization parameter and/or hardness of the radiation field for a given gas phase N/O abundance, with little dependence on electron density owing to similar critical densities (310 and 510 cm^{-3}, respectively). Several sources at $z = 6$–7 have yielded nondetections (Harikane et al. 2020, Sugahara et al. 2021) or faint emission (Novak et al. 2019, Killi et al. 2023, Litke et al. 2023) to date in contrast to bright [OIII] λ88 μm detections. The limits on the [NII]/[OIII] line ratio suggest $\log U_{ion} \gtrsim -3$, which is fully consistent with measurements of the ionization parameter in high-redshift galaxies with JWST (e.g., Reddy et al. 2023). Novak et al. (2019) detect [NII] λ122 μm alongside constraints on [NII] λ205 μm in a quasar host galaxy at $z = 7.5$. The line ratio of the two [NII] lines ([NII] λ122 μm/[NII] λ205 μm > 4.4) gives an electron density constraint of $n_e > 180\,cm^{-3}$, which is consistent with the high electron densities measured by JWST at these redshifts (Isobe et al. 2023, Reddy et al. 2023).

4.4.3. [OI] λ146 μm and [OI] λ63 μm. The neutral oxygen atom has two fine-structure transitions that are accessible to ALMA at $z > 6.5$. [OI] λ63 μm is a bright line in local starburst galaxies ($L_{[CII]}/L_{[OI]} \sim 1$), though it is more difficult to detect at high redshift due to its high frequency, which typically requires ALMA band 9 or 10 observations. [OI] λ146 μm is an ∼10× fainter line but conveniently observable in ALMA band 6 at $z \sim 7$.

Due to the first ionization potential of oxygen being identical to hydrogen (13.6 eV), the [OI] fine-structure lines trace the neutral ISM without being affected by ionized gas. Both [OI] lines have a higher critical density than [CII] λ158 μm (∼10^5 cm^{-3} versus ∼10^3 cm^{-3} in neutral gas) and a higher excitation temperature needed to populate the upper level (228–329 K versus 91 K); therefore, [OI] traces warmer, denser gas than [CII], and their line ratio gives important insight into the ISM conditions of the star-forming gas within galaxies.

No robust detections of [OI] λ63 μm have been obtained at $z > 6.5$ to date (Rybak et al. 2023), though Ishii et al. (2025) detect the line at $z = 6.04$ in a quasar host galaxy with $L_{[CII]}/L_{[OI]} = 1.3 \pm 0.5$, which is consistent with local starburst galaxies. New detections of bright, very high-redshift galaxies with JWST might enable observations in ALMA bands 7–8 for similar line strengths in the near future. Promisingly, several detections of [OI] λ146 μm in LBGs (Fudamoto et al. 2024), an SMG (Litke et al. 2023), and a quasar (Novak et al. 2019) are now obtained at $z > 6.5$. In all these galaxies a remarkable high [OI]/[CII] ratio has been established compared to the local galaxy population (including starbursts, metal-poor dwarfs, and AGNs), suggesting the ISM in high-redshift galaxies is systematically denser ($\sim$10−1,000×) than MS galaxies at $z \sim 0$.

The [OIII] λ88 μm/[OI] λ63 μm or [OIII] λ88 μm/[OI] λ146 μm ratio, which is insensitive to variations of elemental abundances, may be used as an indicator of the filling factor of ionized gas, traced by [OIII], relative to the filling factor of PDRs, traced by [OI] (Cormier et al. 2015). The bright detections of [OI] λ146 μm to date compared to [OIII] λ88 μm suggest similar PDR filling factors as local (U)LIRG galaxies but significantly higher PDR filling factors than local metal-poor dwarf galaxies (Fudamoto et al. 2024).

4.4.4. [NIII] λ57 μm. The double ionized nitrogen ion has a fine-structure transition [NIII] λ57 μm that falls in ALMA band 9 at $z \sim 7$. The most promising use of [NIII] λ57 μm is in combination with [OIII] λ88 μm or [OIII] λ52 μm to derive N/O abundance. Oxygen is an alpha-capture primary element produced by massive stars, whereas nitrogen is both a primary and a secondary nucleosynthetic element. Furthermore, oxygen and nitrogen have similar ionization potentials, making their line ratios only weakly dependent on ionization parameter and radiation hardness. Therefore, the [NIII]/[OIII] ratio is a good proxy for N/O relative abundance, which provides constraints on the SFH of the galaxy, and can be calibrated as a metallicity indicator (e.g., Peng et al. 2021).

Both Nagao et al. (2011) and Pereira-Santaella et al. (2017) present [OIII]/[NIII] λ57 μm-based metallicity calibrations using `Cloudy` modeling. These models suggest [NIII] is reasonably bright ($L_{[\mathrm{OIII}]88} \sim L_{[\mathrm{NIII}]57}$) at solar metallicity, but for lower-metallicity systems it becomes too faint for the lower-sensitivity bands of ALMA. However, recent JWST observations report the existence of N-emitters—sources with (super-)solar N/O despite subsolar O/H abundance (e.g., Cameron et al. 2023, Castellano et al. 2024). These sources could be bright in [NIII] λ57 μm and particularly interesting at $z > 10$, where the line moves into ALMA band 8.

4.4.5. CO and [CI]. At $z \sim 7$, rotational CO transitions $J = 3$–2, 6−7, and higher are accessible with ALMA owing to the recent installment of band 1 receivers. Furthermore, the neutral gas tracer [CI] has two fine-structure lines close to CO(4–3) and CO(7–6) in frequency. However, due to their inherent faintness, studies remain limited to IR-bright systems, such as SMGs or quasar host galaxies. Jarugula et al. (2021) detect CO $J = 6$–5, 7–6, 10–9, and [CI] λ370 μm in two SMG-selected galaxies at $z = 6.9$. They derive a CO ladder that peaks at $J = 6-5$ and steadily declines toward higher J transitions. From the CO-based gas mass measurements, there is no evidence for evolution in depletion time, which is consistent with [CII]-based results in LBGs at the same redshift (Aravena et al. 2024). Venemans et al. (2017), Decarli et al. (2022), and Li et al. (2022) detect high-J CO lines and [CI] 370 μm in quasar host galaxies at $z > 6.5$, whereas Kaasinen et al. (2024) detect CO(2–1) with the Jansky Very Large Array (JVLA) in three of them. The [CII]/[CI] ratio is particularly useful for differentiation between PDRs and XDRs (X-ray-dominated regions), with all quasar host galaxies preferring the PDR ISM conditions, which suggests that the central black holes of these galaxies do not significantly impact the cold ISM. The CO ladder rises strongly from CO(2–1) to CO(6–5) and CO(7–6), suggesting a significant fraction of gas is in a high-excitation state.

In less luminous systems, Hashimoto et al. (2023b) target an LBG at $z = 7.15$ and find nondetections for CO(6–5), CO(7–6), and [CI] 370 μm. Their limits on $L_{[\mathrm{CII}]}/L_{\mathrm{CO}}$ are higher than those found in quasar host galaxies and suggest lower density in the PDR gas. Jones et al. (2026) use the JVLA to constrain CO(2–1) in an LBG at $z = 8.31$. The most distant successful detection of CO in an LBG is currently at $z = 7.31$ (Cescon et al. 2026).

5. DUST CONTINUUM

There remain fundamental open questions in the study of dust in the early Universe. When did significant dust accumulate in the Universe? How does the dust differ from that found in local galaxies? How important is dust-obscured star formation in the census of galaxies in the early Universe? Here, we describe the key observational constraints on the dust continuum emission to date at $z > 6.5$ and discuss the implications of these measurements on the obscured component of cosmic star-formation and dust formation mechanisms.

Obscured fraction: $f_{\rm obs} = \frac{\rm SFR_{IR}}{\rm (SFR_{UV}+SFR_{IR})}$

5.1. The Fraction of Obscured Star Formation

The importance of dust-obscured star formation in galaxies can be quantified by measuring $f_{\rm obs}$, the fraction of obscured star formation. At $z \lesssim 2$, a stellar mass and SFR dependence on $f_{\rm obs}$ has been observed. Do such relations exist at $z > 6.5$?

5.1.1. $f_{\rm obs}$–$M_\star$. The majority of sources in our compilation have upper limits on their dust continuum emission from ALMA or NOEMA as shown in **Figure 8**. To mitigate this, several stacking analyses have been performed to determine an average $f_{\rm obs}$ in high-redshift galaxy samples. For the REBELS sample, we show the stacking results from Algera et al. (2023) at $z \simeq 7$ and compare them to the results at $z = 4$–6 from the ALPINE survey presented by Fudamoto et al. (2020). To complement these targeted results on relatively high-mass galaxies, deep-field programs provide stacked constraints on the $f_{\rm obs}$ of lower-mass galaxies. The Bouwens et al. (2020) results, derived in a broad redshift bin ($z = 3.5$–10), appear to indicate that galaxies at $\log_{10}(M_\star/{\rm M}_\odot) \simeq 8$–$9$ show a relatively low obscured fraction of $\sim$20%, which is consistent with the lack of dust continuum detections found within the ASPECS survey. Similar results are found from the stacking results of Ciesla et al. (2025), who included spectroscopically confirmed sources in the $\rm A^3$COSMOS data.[4]

Taking together the individual sources and the stacking results, there is evidence for a trend in $f_{\rm obs}$ with stellar mass at $z > 6.5$. We compare the $z > 6.5$ results to the studies of Whitaker et al. (2017) and Shivaei et al. (2024) at $z = 0$–2.5. Whitaker et al. (2017) performed a stacking analysis of a sample of mass complete SDSS (Sloan Digital Sky Survey) galaxies, with the FIR emission being derived from the *Spitzer*/MIPS (Multiband Imaging Photometer) 24-μm band and assuming a conversion from this band to the full $L_{\rm IR}$. Shivaei et al. (2024) instead derived the obscured fraction of star formation from SED fitting of MIRI (Mid-Infrared Instrument)-selected sources at $z = 0.7$–2 with coverage of the PAH (polycyclic aromatic hydrocarbon) features (which are used to estimate the $L_{\rm IR}$) at around $\lambda_{\rm rest} = 6$–11 μm. Both of these studies see a trend with increasing $f_{\rm obs}$ with stellar mass, with a large scatter around the relation. Whitaker et al. (2017) find no evolution with redshift (up to $z = 2$) in the $f_{\rm obs}$–$M_\star$ relation, which is supported by the Shivaei et al. (2024) results. The results presented here suggest that there is an evolution of the relation to lower $f_{\rm obs}$ at a given stellar mass at $z > 6.5$. Algera et al. (2023) and Fudamoto et al. (2020) showed that while the Whitaker et al. (2017) study would predict $f_{\rm obs} > 0.8$ for the ALPINE and REBELS galaxies at $\log_{10}(M_\star/{\rm M}_\odot) \simeq 10$, instead the fraction is lower at around $f_{\rm obs} \sim 0.45$.

[4]Note that these studies assume different FIR SEDs compared to the default in this review, with the REBELS analysis assuming the constant conversion factor used by Inami et al. (2022) and ALPINE assuming the template of Béthermin et al. (2020). In addition, Algera et al. (2023) excluded starbursts. Bouwens et al. (2020) assumed $\beta_{\rm d} = 1.6$ and an evolving dust temperature. To show the $f_{\rm obs}$ derived from the ASPECS program by Bouwens et al. (2020) at $\log_{10}(M_\star/{\rm M}_\odot) < 9$, we converted the provided IRX value. We refit the Ciesla et al. (2025) fluxes with the same FIR SED as that used in this review.

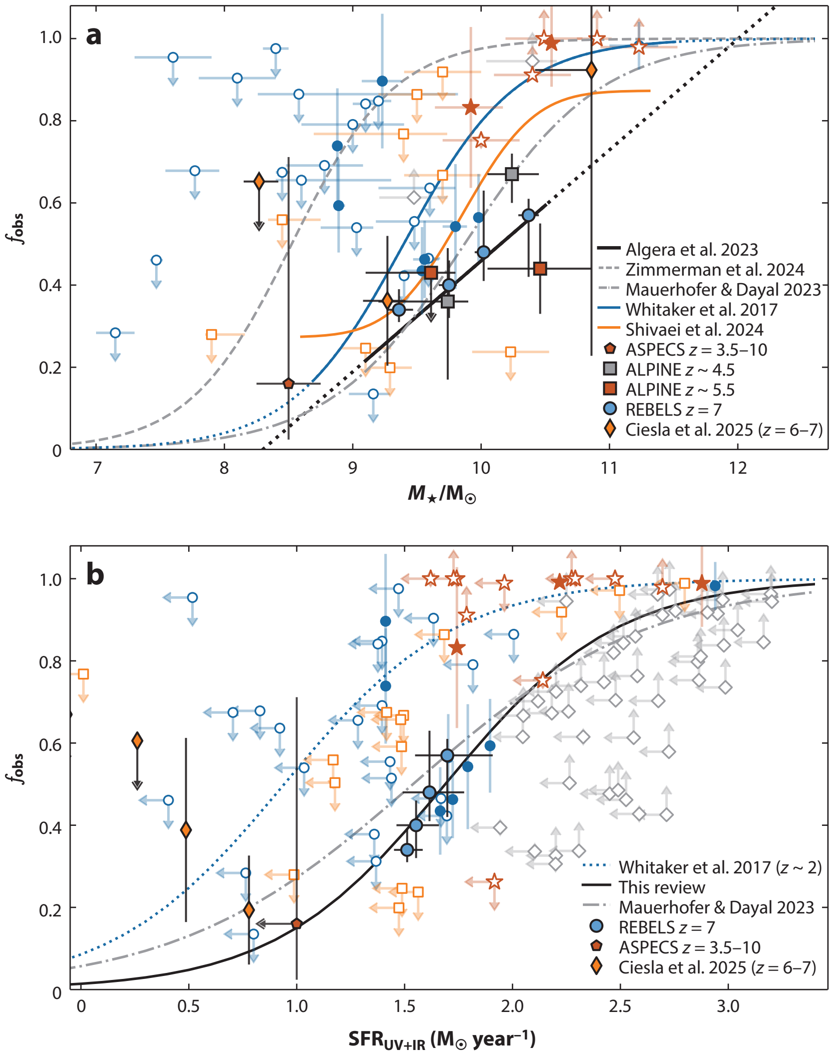

Figure 8

The obscured fraction of star formation as a function of (*a*) stellar mass and (*b*) total SFR. In both panels, the open symbols correspond to objects for which there is a limit set as 3σ, placed on either the UV or far-IR SFR (i.e., a nondetection). (*a*) We show a subset of sources that have $M_\star$ measurements. We also show the stacked results from the REBELS survey (Algera et al. 2023), the ALPINE survey (Fudamoto et al. 2020), the ASPECS survey (Bouwens et al. 2020), and A^{3}COSMOS (Ciesla et al. 2025). (*b*) The $f_{\rm obs}$ as a function of total SFR (with our best-fit relation following Equation 13). Abbreviation: SFR, star-formation rate.

It is clear in **Figure 8** that there is a large scatter for individual objects around the relations derived from, for example, the REBELS results (Algera et al. 2023). One significant part of the scatter is likely due to sample selection effects, as can be seen by comparing the $f_{\rm obs}$ for LAEs and ALMA-selected sources. LAEs show exclusively upper limits, with a group of three sources at $\log_{10}(M_\star/{\rm M}_\odot) \sim 10$ with very low obscured fractions of star formation ($f_{\rm obs} \lesssim 0.25$), as expected given the expected low dust content in these sources (Ouchi et al. 2020). Conversely, the ALMA-selected serendipitous sources from Fudamoto et al. (2021), which are spectroscopically confirmed via [CII], show extremely high f_{obs} as expected from their lack of rest-frame UV emission.[5] We note that if stellar masses are underestimated as some resolved studies and studies using nonparametric SFHs are suggesting at $z > 6$ (e.g., Giménez-Arteaga et al. 2023), then the offset to the f_{obs} predicted by the $z \simeq 2$ studies would increase. Similarly, if the dust temperature is lower on average than the value we assume, then the f_{obs} offset would also increase compared to $z \simeq 2$.

Infrared excess: $IRX = L_{IR}/L_{UV}$

5.1.2. f_{obs}–SFR. Although the trends in f_{obs} have been discussed mainly with respect to stellar mass, further information can be gathered from the relation as a function of total SFR ($SFR_{UV+IR} = SFR_{UV} + SFR_{IR}$). As a greater proportion of the ALMA compilation has UV+IR measurements (including the quasars), this diagram is populated by an increased number of sources. Unsurprisingly, the LAEs show low f_{obs} values, which populate the lower right-hand side of **Figure 8**; which FIR-detected sources appear to be highly star-forming; and obscured objects. There are also clear selection effects on the population of the diagram, with the REBELS sample of LBGs (which makes up the majority of the central points), are UV bright and, hence, have $\log_{10}(SFR_\star/M_\odot\ year^{-1}) > 1.5$ by prior selection, with upper limits on the dust-obscured component in most cases. We also show the stellar mass binned f_{obs} values from Algera et al. (2023) converted into SFR_{UV+IR} bins using the average M_{UV} of the REBELS sample (to give the UV SFR). The stacking results from Ciesla et al. (2025) were converted to total SFR assuming the same conversions as this review.

For the quasar host galaxies, we show these sources on the f_{obs}–SFR diagram only, as it is challenging to measure the stellar mass from the quasar-dominated rest-frame UV and optical emission. If we assume that the quasar host accounts for less than 10% of the UV emission, we can put a limit on f_{obs}. With this assumption, these values support quasar hosts being extremely dust obscured ($f_{obs} > 0.5$) with high total SFRs on the order of $\simeq$100–1,000 $M_\odot\ year^{-1}$, as identified in previous works (e.g., Venemans et al. 2020).

Notwithstanding the multiple limits and sample selection effects that go into **Figure 8**, there is evidence for a trend in the f_{obs} with total SFR. As shown in **Figure 8**, the f_{obs} from the stacked results shows a deficit with respect to the $z \simeq 2$ trend from Whitaker et al. (2017). Whitaker et al. see a trend to decreasing f_{obs} at a given SFR from $z = 0$–2. The results at $z > 6.5$ show a continuation of this trend, such that at a given SFR_{UV+IR}, a smaller proportion of the total SFR is obscured at higher redshift. Following these lower-redshift studies, we find that a functional form of

$$f_{obs} = \frac{1}{(1 + a\, e^{b\,SFR})}, \qquad 13.$$

with $a = 70$ (compared to $a = 10.7$ at $z = 2$) and $b = -2.5$ (fixed to the $z = 2$ value), can well describe the data at $z > 6.5$, although there is significant scatter. This form closely follows that found by the model predictions as illustrated in **Figure 8** for the f_{obs}–$M_\star$ relation (and infrared excess—see Section 5.2). Using a cosmological hydrodynamic simulation with on-the-fly dust formation (including dust evolution and destruction), Zimmerman et al. (2024) overpredicts the f_{obs} at high-redshift in comparison to the observations. In contrast, the Mauerhofer & Dayal (2023) semianalytic model shows good agreement; however, this model assumes perfect mixing of gas and dust and a uniform spherical dust geometry. Zimmerman et al. (2024) attribute their predicted increase in f_{obs} at a given stellar mass to the compact sizes and higher gas fractions in galaxies at higher redshift, pointing out that observations may be biased low due to selection effects.

[5] We note that the stellar masses for both LAEs and the serendipitous sources can be uncertain owing to a lack of detections in the rest-frame UV and optical bands.

5.2. Infrared Excess Scaling Relation

The importance of dust obscuration has been further quantified in the literature using the IRX–β and IRX–$M_\star$ relations. IRX is defined as the logarithm of the ratio of the total IR to monochromatic UV luminosity. It combines the rest-frame UV and FIR parts of the galaxy SED, providing additional information on the dust properties [e.g., the rest-frame UV can give attenuation curves (see Salim & Narayanan 2020), but cannot discern geometrical offsets between stars and dust]. We present the IRX–$M_\star$ relation in **Supplemental Figure 5**, because it can be directly related to the f_{obs} relations discussed in Section 5.1.

Supplemental Material >

The IRX has been shown to form a tight correlation with galaxy color in the rest-frame UV (β_{UV}) in starburst galaxies in the local Universe (Meurer et al. 1999), which is as expected if the energy lost in the rest-frame UV is reradiated in the FIR (Calzetti et al. 2000). Deviations above the relation have been shown in various theoretical and observational works to be caused by geometrical offsets between the unobscured regions (leading to blue $\beta_{\mathrm{UV}} \simeq -2$ but a large IRX that is dominated by fully obscured regions). Conversely, deviations below the relation can be a result of older stellar ages or a steeper attenuation curve (see, e.g., Popping et al. 2017a, Vijayan et al. 2022). Initial observations with ALMA and NOEMA at $z \sim 5$ by Capak et al. (2015) revealed red galaxies with a low IRX, indicating low dust-obscured SFR and suggestive of a Small Magellanic Cloud (SMC)-like (hinting at low-metallicity) extinction curve. ASPECS results similarly suggested a deficit in IRX at a given β_{UV} from stacking results (in the range of $z = 3.5$–10) (Bouwens et al. 2020). The ALMA Frontier Fields Survey (FFS) produced only upper limits in stacking results from Carvajal et al. (2020), with the highest-redshift sources at $z = 5$. Studies following-up brighter $z \simeq 7$ galaxies recovered a range of values supporting a deficit (Smit et al. 2018, Hashimoto et al. 2019) or finding some consistency with the local starburst relation (Bowler et al. 2018, Schouws et al. 2022).

We show the ALMA compilation on the IRX–β relation in **Figure 9**, where we split by redshift for clarity (at $z = 7.7$). It is clear that the majority of galaxies do not have a dust continuum detection. The majority of sources are also relatively blue, with $\beta_{\mathrm{UV}} \simeq -2$, potentially due to the LBG selection process (which favors blue sources over redder objects that are more likely to be confused with contaminant populations). Interestingly, there are several $z > 7.7$ sources that show redder slopes $\beta_{\mathrm{UV}} \simeq -1.2$, including the highest-redshift dust detection (MACS0416-Y1) (Ma et al. 2024, Harshan et al. 2024). This could be a result of reduced blue bias in the sample selection for certain spectroscopic follow-up campaigns with JWST. Quasar hosts cannot be accurately represented as the rest-frame UV emission is dominated by AGN emission. With the assumed FIR SED of this work, we see that there are sources both above and below the low-redshift Calzetti-like relation. Bowler et al. (2024) performed a stacking analysis of the REBELS and ALPINE sources, assuming a $T_{\mathrm{d}} = 46\,\mathrm{K}$ and $\beta_{\mathrm{d}} = 2.0$ from $z = 4$–8. They found consistency with the local Calzetti et al. (2000) starburst relation on average for galaxies at these redshifts. This suggests little evolution in the dust properties of galaxies from the local Universe; however, we note that the attenuation properties are only weakly related to the underlying extinction curve once a complex geometry is taken into account (Narayanan et al. 2018). There remain a handful of sources below the SMC-like extinction curve prediction in the IRX–β diagram at $z = 6.5$–7.7. This could be interpreted as evidence for an SMC-like attenuation curve.

At $z > 7.7$, the errors on β_{UV} are generally reduced, due to the availability of JWST spectra. A handful of these high-redshift sources also show a deficit in comparison to the REBELS/Calzetti-like prediction (ID4590, MACS0416-Y1), suggesting that if the FIR SED assumptions are realistic, dust properties may be different in the very early Universe. However, the key uncertainties in this measurement are (*a*) the assumed FIR SED, as temperature changes can cause great changes in

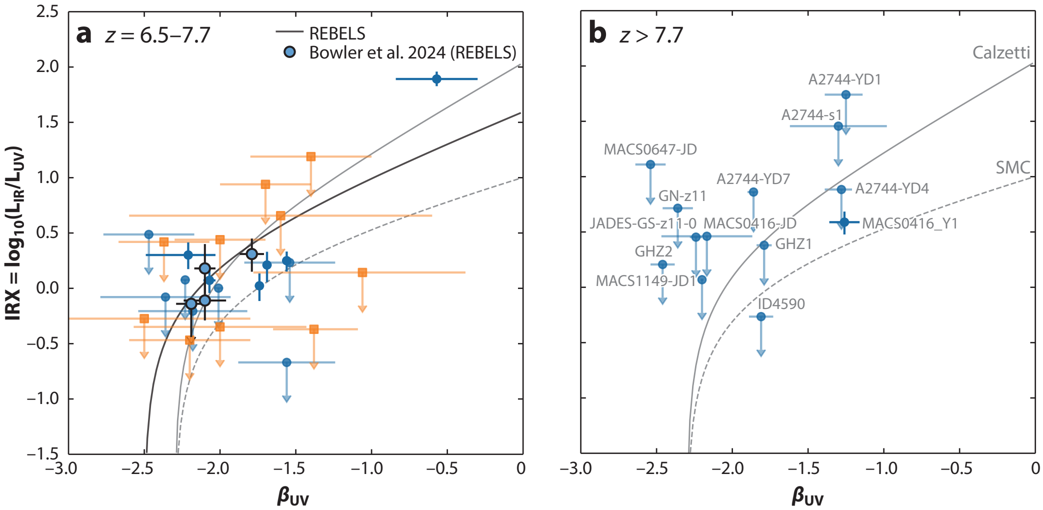

Figure 9

The IRX–β relation with rest-frame UV slope taken from the compilation of ALMA observed sources at (*a*) $z = 6.5$–7.7 and (*b*) $z > 7.7$. We compare to the local prediction from the Calzetti et al. (1994) attenuation law and the SMC extinction law, assuming a screen of dust. For clarity, the majority of REBELS galaxies have been removed from the plot, and the stacked results from Bowler et al. (2024) are shown instead (*open circles*). REBELS galaxies that have improved β_{UV} values from the *James Webb Space Telescope* are shown separately (Fisher et al. 2025). Abbreviations: ALMA, Atacama Large Millimeter/submillimeter Array; IRX, infrared excess; REBELS, Reionization Era Bright Emission Line Survey; SMC, Small Magellanic Cloud.

the derived L_{IR} and, hence, IRX, and (*b*) errors on the slope β_{UV}, which, while mitigated by JWST spectroscopy, are still dependent on calibrations and the method used to derive the slope. Finally, there is the uncertain effect of stardust geometry and the unknown intrinsic UV-slope of these galaxies. Further deep multiband ALMA observations are required to define this relation at $z \gtrsim 8$.

Several simulations and models predict an excess in the IRX–β relation at $z > 6.5$ in comparison to the local relation (Ferrara et al. 2022, Pallottini et al. 2022), whereas others predict little evolution to higher redshifts (Narayanan et al. 2018, Liang et al. 2021, Vijayan et al. 2022, Mauerhofer & Dayal 2023) or a deficit as expected for the SMC-like dust (Ma et al. 2019). Narayanan et al. (2018), for example, predict an attenuation curve close to the Calzetti et al. (2000) form, due to sources having a complex stardust geometry (which tends to flatten the law) as well as a smaller range in the intrinsic ages of galaxies at high redshift.

5.3. Cosmic Star-Formation Rate Density

As discussed so far, the direct detection of the dust continuum emission provides an estimate of the obscured SFR in galaxies. This can be used to compute the obscured cosmic star-formation rate density (CSFRD), typically by using an estimation of the IR luminosity function (LF), which can then be integrated down to a particular limiting L_{IR} and transformed into a CSFRD via an L_{IR}-to-SFR_{IR} conversion factor. Due to the dependence on stellar mass of the f_{obs}, coupled with the small field of view of ALMA/NOEMA, it is challenging to determine the IR LF from blind surveys that have small numbers of detections (if any at high redshift). Instead, the IR LF is typically inferred from combining the rest-frame UV LF or the galaxy stellar mass function (GSMF) as a basis for the number density of sources, with a relation between the L_{IR} and M_{UV} or $\log_{10}(M_\star/M_\odot)$. As this is highly survey-dependent, we do not compute this for the sources in our compiled catalog but instead look to the literature for estimates.

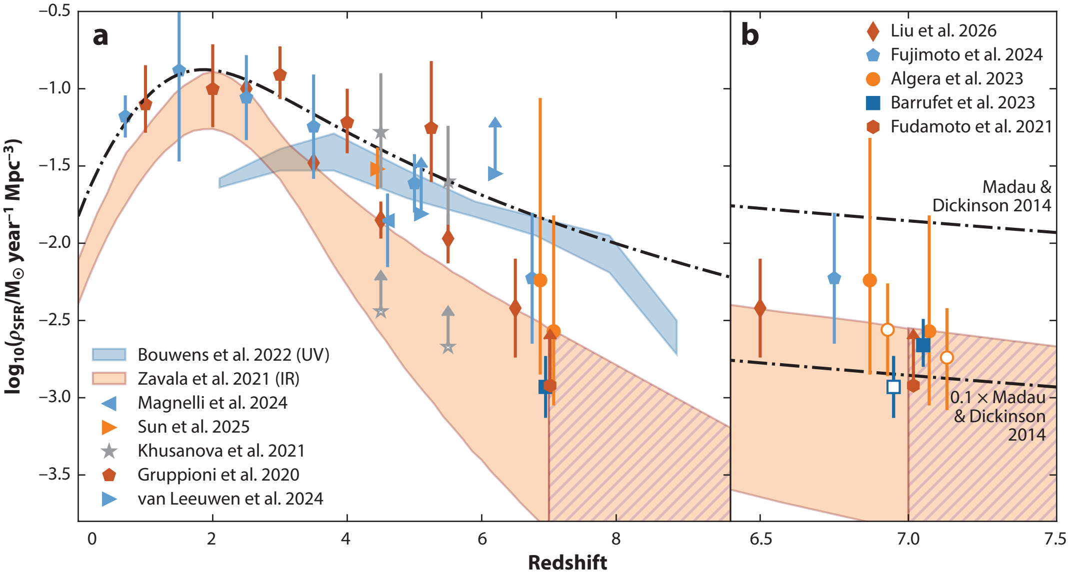

Figure 10

(*a*) The cosmic SFR density as a function of redshift. We show estimates of the obscured CSFRD determined for galaxies at $z > 6.5$ from Algera et al. (2023), Barrufet et al. (2023), Fudamoto et al. (2021), Fujimoto et al. (2024), and Liu et al. (2026). These are shown in comparison to the total expected value from Madau & Dickinson (2014) (*dot-dashed line*), the UV (unobscured) measurement from Bouwens et al. (2022), and the IR (obscured) model from Zavala et al. (2021). (*b*) A zoom-in of the high-redshift results. The open points represent measurements from Algera et al. (2023) and Khusanova et al. (2021) without extrapolation to lower stellar masses than the REBELS (ALPINE) sample and, hence, represent a lower limit. The open points from Barrufet et al. (2023) are when the serendipitous sources from Fudamoto et al. (2020) are removed. Abbreviations: CSFRD, cosmic star-formation rate density; SFR, star-formation rate.

Algera et al. (2023) used the REBELS sample to determine the CSFRD at $z \simeq 7$, using the GSMF coupled with a stacking analysis, to determine a relation between stellar mass and IR luminosity. The slope of this relation was sensitive to how binning was performed, and hence we present two points in **Figure 10** corresponding to the Monte Carlo and simple binning approaches in this study. The integral to compute the CSFRD was computed to the point at which Algera et al. (2023) determine the f_{obs} is consistent with zero ($\log_{10}(M_\star/\mathrm{M}_\odot) \sim 8.2$). We also present the results when only the stellar mass range of the REBELS galaxies themselves is considered. An independent estimate of the CSFRD from the REBELS sample was derived by Barrufet et al. (2023), who determined the IR LF by instead determining the number density of sources from the UV LF. The IR LF is still weakly constrained at $z \simeq 7$; however, Barrufet et al. (2023) were able to measure three LF points across the expected knee [$\log_{10}(L_{\mathrm{IR}}/\mathrm{L}_\odot) = 11.4$–$12.12$, with the knee at around $\log_{10}(L_{\mathrm{IR}}/\mathrm{L}_\odot) = 11.6$]. The faint-end slope was fixed to $\alpha = -1.3$, and they integrated down to $L_{\mathrm{IR}} = 10^{10.5}\ \mathrm{L}_\odot$. From these REBELS analyses, the obscured CSFRD is measured to be at least 10% of UV-based estimates (see **Figure 10*b***).

The ACLS has been used to estimate the IR LF up to $z \simeq 7$ (Fujimoto et al. 2024). This survey found a single galaxy at $z > 6$, the Cosmic Grapes source at $z = 6.07$. With this galaxy, and estimates from other sources in the literature, Watson et al. (2015), Fudamoto et al. (2021), and Barrufet et al. (2023) compute the IR LF at $z = 6$–7.5 and, subsequently, the obscured CSFRD at this epoch. The faint-end slope was fixed to $\alpha = -0.94$, and they integrated down to $L_{\mathrm{IR}} = 10^{10}\ \mathrm{L}_\odot$. We show their obscured estimates in **Figure 10**. When they add these values to the unobscured component as determined by Bouwens et al. (2022), the result is around 60% in excess of Madau & Dickinson (2014); however, multiple uncertainties remain in the computation of the IR LF. These include the conversion of L_{IR} to SFR_{IR}, the computation of L_{IR} from a single data point in the FIR, and the small number statistics at $z > 4$ (where only 13 galaxies are detected in an area of 100 arcmin^2). Liu et al. (2026) performed a stacking analysis of the A^{3}COSMOS data in the PRIMER (Public Release IMaging for Extragalactic Research) COSMOS field to determine the obscured CSFRD from $z = 3$–7, estimating that ∼20% of the CSFRD can be obscured even at $z \simeq 7$. We show their estimate from all massive galaxies in the COSMOS field, using the average relation between sSFR and L_{IR} to include sources in the estimate even if they are not covered by ALMA data. A lower limit on the obscured CSFRD from serendipitous sources was estimated from early REBELS data by Fudamoto et al. (2021), who discovered two [CII]-detected but HST-dark galaxies in the LBG-targeted ALMA pointings. They computed the CSFRD by taking the volume of the REBELS ALMA data available at that point, and the SFR estimates from the UV and IR luminosities (the results are consistent if [CII] SFRs are used instead). The CSFRD was then corrected by a factor of four to account for the clustering of the sources.

We compare several estimates of the obscured CSFRD at $z = 4$–6, where several studies have suggested the obscured contribution could be dominant, although there is large scatter. From ALPINE we show the results from Khusanova et al. (2021), who used stacking to obtain a L_{IR}-to-M_{UV} or stellar mass relation for the main sample, and Gruppioni et al. (2020), who searched for serendipitous sources. The dependence on extrapolating beyond the range of the data can be seen, for example, in the two sets of Khusanova et al. (2021) points presented in **Figure 10**. We show the results from van Leeuwen et al. (2024), who looked for serendipitous sources in the REBELS and ALPINE data (including the results in Loiacono et al. 2021). From A^{3}COSMOS, we present the results from Magnelli et al. (2024) and Liu et al. (2026), and from ASPIRE we show the results of Sun et al. (2025) determined from eight serendipitous sources at $z = 4$–6 around the targeted $z > 6.5$ quasars. Zavala et al. (2021) extrapolated the IR LF and evolution determined from the MORA survey to predict that 20–25% of the CSFRD at $z = 6$–7 should be obscured.

Although there remain uncertainties in the computation of the CSFRD at $z > 6.5$, it is clear that even with conservative assumptions (e.g., Algera et al. 2023), there is a significant component (>10%, and up to 40%) that is obscured. As we have shown in earlier sections, there is a stellar mass and SFR dependence of the f_{obs}, and hence this obscured component is mainly contributed by galaxies at $\log_{10}(M_\star/M_\odot) > 9$ and $SFR_{UV+IR} > 10\,M_\odot\,year^{-1}$. The obscured component of the CSFRD at $z > 7$ remains poorly constrained with the lack of sufficiently deep data on samples of galaxies at these redshifts. However, considering the extrapolation of the Zavala et al. (2021) and Madau & Dickinson (2014) relations, we could expect on the order of 10% to still be obscured at $z \simeq 8$.

5.4. Dust Temperature

With the advent of multiband ALMA measurements, it has become possible to place constraints on the FIR SED shape, in particular, the dust temperature (and in some cases emissivity) at very high redshifts. Doing this requires a minimum of two bands (typically band 6 and band 8 at $z \simeq 7$, as these bands can also be used to target the redshifted [CII] and [OIII] lines, respectively). **Figure 11** shows a compilation of T_d measurements at $z \gtrsim 5$ in comparison to several empirical and simulation predictions for the T_d evolution. At $z > 6.5$ there are 11 galaxies, 2 quasars, and 2 SMGs (in the same system—SPT (South Pole Telescope)-E and SPT-W) at the time of writing that have published T_d measurements from multiband observations. An early compilation was made by Witstok et al. (2022), who fitted a sample of five LBGs that had constraints in bands 6

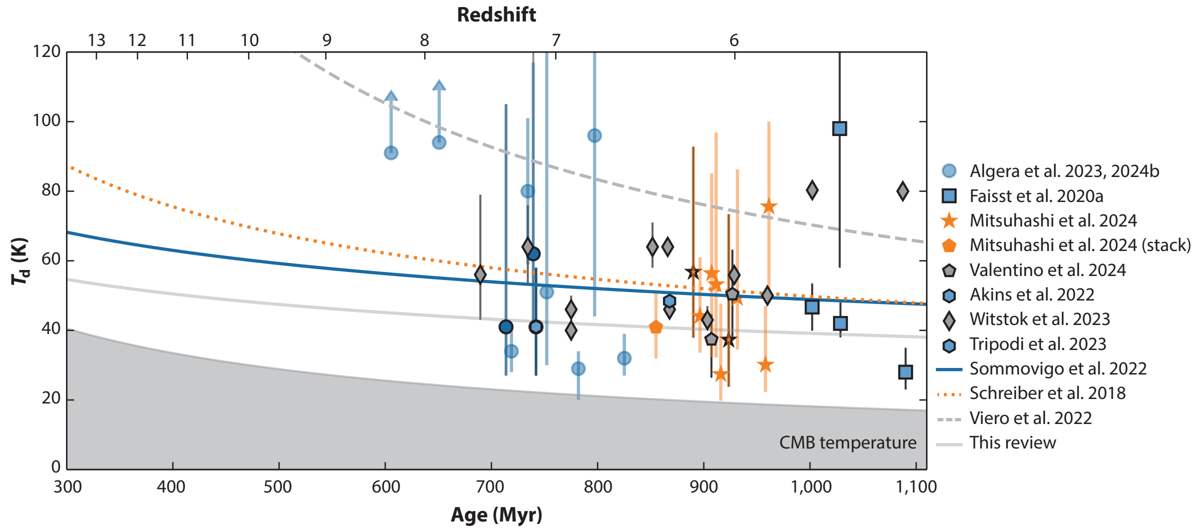

Figure 11

The measured spectral energy distribution dust temperature from galaxies with multiband Atacama Large Millimeter/submillimeter Array observations. The $z > 6.5$ constraints are from Algera et al. (2023), taking the values with $\beta_\mathrm{d} = 2.0$. Sources with detections in >2 bands in the far-IR are outlined in black. Mitsuhashi et al. (2024) provided measurements from the SERENADE sample at $z \simeq 6$, where they allowed β_d to be free in the fitting. We also show the Cosmic Grapes source studied by Valentino et al. (2024). The values for the four sources studied by Faisst et al. (2020a) (who compiled band 6, 7, and 8 data) are taken from Algera et al. (2023), assuming $\beta_\mathrm{d} = 2.0$. Abbreviations: CMB, cosmic microwave background.

and 8. COS-3018, REBELS-P9, and REBELS-P7 have detections and showed a wide range of dust temperatures ($T_\mathrm{d} = 30$–$100\,\mathrm{K}$). COS-2987 and Z-007 were not detected in any ALMA band and, hence, T_d was not constrained. Algera et al. (2024b) performed fitting of three REBELS sources (REBELS-12, 25, and 38) that have band 6 and band 8 observations, plus they presented a refitting of other sources using a consistent fixed $\beta_\mathrm{d} = 2.0$. They instead found low dust temperatures of $\sim$30 K, which importantly increases the derived dust masses (see Section 5.5).

Several sources have observations in a large number of bands and, hence, have more precise T_d (and sometimes β_d) measurements. Algera et al. (2024a) fitted data for the IR luminous galaxy REBELS-25 from bands 3, 4, 5, 6, 8, and 9. The resulting temperature of $T_\mathrm{d} = 32^{+9}_{-6}$ (and $\beta_\mathrm{d} = 2.5 \pm 0.5$) supports a lower dust temperature. The B14-65666/Big Three Dragons source has a fitted temperature of $T_\mathrm{d} = 62^{+55}_{-23}$, wherein the lack of a turnover in the FIR bands to lower wavelength results in greater errors than for REBELS-25. A $T_\mathrm{d} = 41^{+17}_{-14}\,\mathrm{K}$ and $\beta_\mathrm{d} = 1.7^{+1.1}_{-0.7}$ was found for the A1689–zD1 (Akins et al. 2022), which is consistent with the fitting for the same source of Bakx et al. (2021). It has observations in bands 3, 6, 7, 8, and 9, with a good constraint on the peak of the SED. Surprisingly, two $z \sim 8$ sources show evidence for extremely high dust temperatures of $>$90 K. MACS-0416-Y1 is a lensed galaxy that has been well studied across multiple bands with ALMA and is currently the highest-redshift dust detection ($z = 8.3113$) (Bakx et al. 2020). The measurements for galaxy A2744-YD4 ($z = 7.88$) (Laporte et al. 2017, Hashimoto et al. 2023a) are also consistent with a high dust temperature; however, it only has 3–4σ detections in bands 6 and 7 (Algera et al. 2024b). The compact galaxy/quasar hybrid source found at $z = 7.19$ presented by Fujimoto et al. (2022) has a measured high dust temperature ($T_\mathrm{d} \sim 80\,\mathrm{K}$), as do the other quasar host galaxies presented by, e.g., Novak et al. (2019) and Venemans et al. (2020). Note that the dust temperature when the peak is not constrained is degenerate with the emissivity index, such that a lower β_d results in a higher temperature (see Sugahara et al. 2022 for an example). Furthermore, typical fits assume optically thin dust; however, if the wavelength at which the dust becomes optically thick (λ_0) approaches the expected peak of the FIR emission, this can also bias the derived temperature (typically to higher values).

At slightly lower redshifts, we show the stacked value from the $z = 6$ SERENADE sample of $T_d = 40.9^{+10.0}_{-9.0}$ (assuming a prior on the emissivity centered on $\beta_d = 1.8$). At $z \simeq 5$, we show the 4 sources with multiband observations from Faisst et al. (2020a) and Villanueva et al. (2024). We show the T_d derived for the $z = 6.327$ quasar presented by Tripodi et al. (2023) from multiband ALMA observations. Witstok et al. (2023) fitted to a compilation of 17 FIR detected sources at $z = 4$–7 that have a minimum of 4 bands in the FIR. They derived an average $\beta_d = 1.8 \pm 0.3$, suggesting little evolution in the effective dust properties from lower redshift (see also Ward et al. 2024) and a mild evolution in the dust temperature.[6]

There remain great uncertainties in the typical T_d of galaxies at $z > 6.5$, and from the data available to date, we cannot discern a strong trend. There are several extrapolations of observed T_d to higher redshifts that predict a rise of different slopes (e.g., Schreiber et al. 2018, Viero et al. 2022). The CMB temperature can become significant in the first billion years, and this leads to a heating of the dust as well as a reduced contrast between the observed continuum emission and the background (da Cunha et al. 2013). It is clear from **Figure 11** that the CMB temperature becomes significant at $z > 8$, where it will exceed 30 K. Models are able to reproduce the evolution with redshift, highlighting the importance of an increasing sSFR or SFR surface density in this rise (Liang et al. 2019, Ma et al. 2019, Sommovigo et al. 2021, Vijayan et al. 2022). They also highlight the effects of a distribution of dust temperatures and multiphase emission (e.g., cold versus warm, mass or luminosity weighted) (e.g., Lower et al. 2024, Sommovigo & Algera 2025). In this review, we assume an offset relation from Sommovigo et al. (2022) that intersects the measured T_d of the SERENADE stack from Mitsuhashi et al. (2024).

5.5. Dust Mass and Dust Formation Mechanisms

The dust mass in galaxies is an important constraint for models of dust production. The relatively short timescales available for dust formation at $z \gtrsim 7$, as well as the different physical conditions in these galaxies (e.g., lower metallicity, compact sizes, higher sSFR), provide a key test and challenge. Several observational constraints have suggested that dust masses at high redshift may be considerable (e.g., Mancini et al. 2016, Leśniewska & Michałowski 2019, Witstok et al. 2022) and potentially in excess of model predictions. The formation of dust at these redshifts is likely to be dominated by core-collapse supernovae (CCSNe), which can rapidly produce dust several million years after the onset of star formation. The impact of AGB stars is thought to be subdominant, owing to the long MS lifetimes of these stars, which results in the delayed production of dust to beyond 150–400 Myrs. Other stellar processes, such as red supergiant stars, produce yields that are too low. See Schneider & Maiolino (2024) for a detailed discussion of production mechanisms. Once created, dust grains are then reprocessed within the ISM. In particular, the role of dust destruction from the CCSN reverse shock is thought to be significant but is highly uncertain. Other processes, such as astration (where dust is trapped within new stars), ejection, and grain growth are also included within models. The relative importance of these processes depends on multiple properties of the galaxy and ISM at high redshift, in particular the IMF (which controls the

[6]Note that due to the requirement of being detected in multiple FIR observations, this sample is biased toward FIR bright ($L_{IR} > 10^{12}$ L$_\odot$) sources, which potentially show higher dust temperatures than those found in lower SFR galaxies.

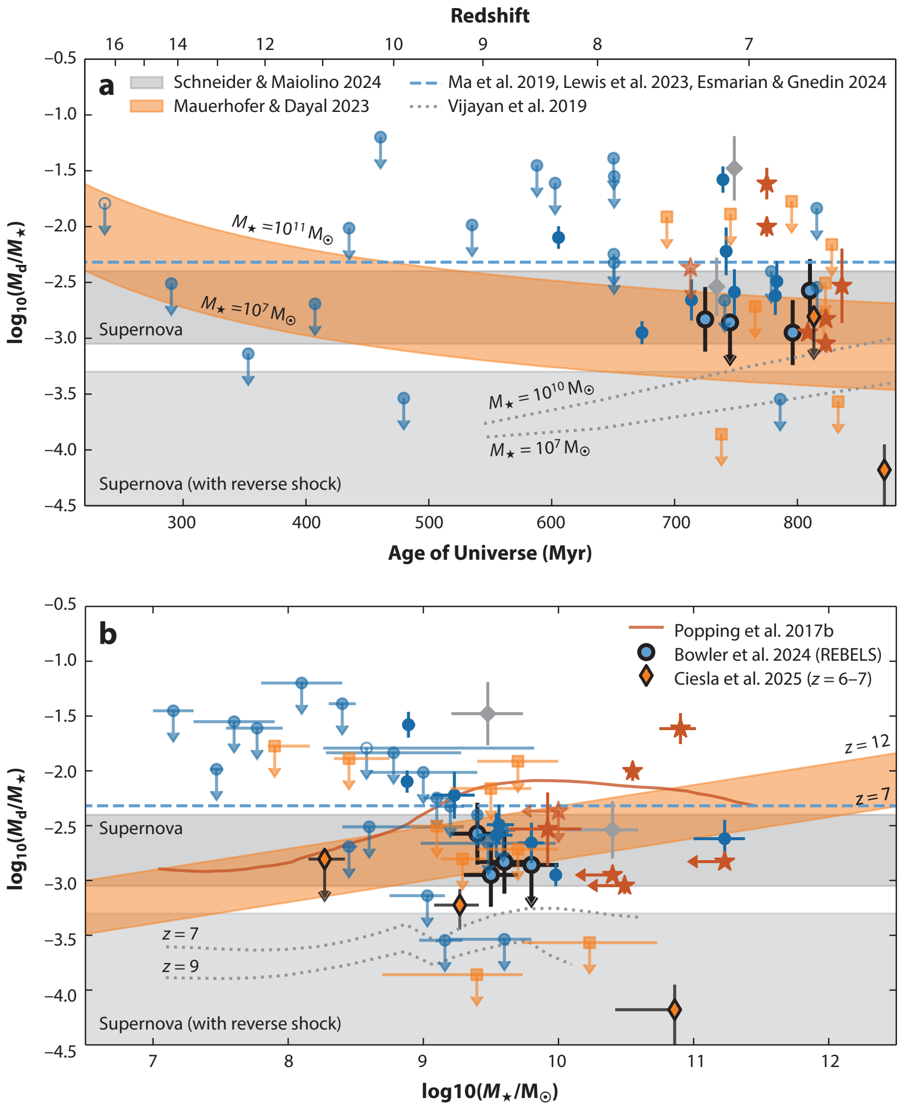

Figure 12

The ratio of the dust mass to stellar mass for the sample of $z > 6.5$ sources. Panel *a* shows this ratio as a function of age, and panel *b* shows this as a function of stellar mass. Predictions of various models and simulations are shown as the different lines. For clarity, the majority of the REBELS galaxies (except those with new *James Webb Space Telescope* stellar masses from Fisher et al. 2025) have been replaced by the stacked results from Bowler et al. (2024). Open symbols represent sources without spectroscopic redshifts.

number of high-mass stars), the stellar and gas phase metallicity (which controls stellar evolution), heating from the CMB, and the SFH. The grain composition and size distribution, as well as the geometry, could also differ (e.g., Narayanan et al. 2025).

In **Figure 12**, we compare the ratio of the dust mass to stellar mass from our compilation to the predictions from models and simulations. We stress here that the dust masses derived at high redshift are subject to several strong systematic uncertainties, namely the dust absorption coefficient and the dust temperature (see Section 5). Furthermore, the stellar masses are uncertain (although to a lesser degree), and the sample selection biases (to UV-bright sources) must be considered. Despite this, we see that the $M_d/M_\star$ for individual sources and stacks are of the same order of magnitude as simulation predictions. In the case of a lower dust temperature (e.g., 25 K for the cold component as advocated in Liang et al. 2019), the dust masses would be significantly higher. Typically, the semianalytic models and simulations produce a constant ratio of $M_d/M_\star$, as the dust mass is related to the CCSN rate, which is correlated with the SFR (and hence the stellar mass for a simple SFH). For example, Ma et al. (2019), Lewis et al. (2023), and Esmerian & Gnedin (2024) all predict an approximately constant ratio of 5×10^{-3}, with ratios in the range of 10^{-3}–10^{-2} common (e.g., Triani et al. 2020, Di Cesare et al. 2023). Some models predict a slight stellar mass dependence, such as that by Popping et al. (2017b). Similarly, Mauerhofer & Dayal (2023) find a weak dependence on stellar mass, related to the higher-redshift halos retaining more gas and dust at a given stellar mass, while Vijayan et al. (2019) see the reverse trend, although the scatter is significantly greater than the difference (shown in **Figure 12**). Some works argue that high stellar yields without significant grain growth can reproduce observations (e.g., Dayal & Ferrara 2018, Triani et al. 2020, Mauerhofer & Dayal 2023), whereas others advocate for the importance of grain growth (e.g., Vijayan et al. 2019, Esmerian & Gnedin 2024).

Predictions for the expected $M_d/M_\star$ can be produced via a relatively simple estimate that takes into account the typical dust yield per stellar event (e.g., per CCSN; y_{SN}) and integrates over a given SFH and IMF. In **Figure 12**, we show the ranges of expected $M_d/M_\star$ from this method as presented by Schneider & Maiolino (2024) (see also Leśniewska & Michałowski 2019, Di Cesare et al. 2023). The AGB predictions from this method are below the vertical range of the plot. The upper range of these predictions, for CCSN without a reverse shock, are in good agreement with the data and the models. However, it is clear that with dust destruction, there is tension with the observations. In particular, the SMG SPT0311-58W is in excess of the predictions by almost an order of magnitude. We conclude that on average the observations are in reasonable agreement with the maximal predictions from models and empirical arguments, especially given the assumptions on both the derived FIR SED and dust formation mechanisms.

6. RESOLVED STUDIES

Although the vast majority of ALMA observations at $z > 6.5$ have been obtained in relatively compact, low angular resolution configurations, they have provided tentative new insights into the sizes, ISM complexity, and kinematics of galaxies. Only recently have higher-resolution ALMA observations been studied, and one of the major challenges for ALMA in the next decades will be to increase the statistical samples of galaxies in which dust and cold gas can be measured on the scales that are now available for stars and hot gas with JWST.

6.1. Morphology

Typically ALMA and NOEMA observations have been at significantly poorer spatial resolution that the available rest-frame UV and optical images. Despite this, measurements of the offset of the rest-frame FIR emission from the stellar emission and the spatial extent have been made.

6.1.1. Offsets. Some of the earliest ALMA observations of $z > 6.5$ galaxies already suggested the possibility of offsets between the rest-frame UV and [CII] emission (e.g., Maiolino et al. 2015, Pentericci et al. 2016), and a significant fraction of $z \sim 5$–6 galaxies showed unambiguous offsets of both the continuum and [CII] emission (Capak et al. 2015, Willott et al. 2015). In contrast,

[OIII] detections have consistently been reported with a good alignment between the UV and line emission (e.g., Inoue et al. 2016, Witstok et al. 2022).

Given the importance of dust in the excitation of [CII] in PDRs, some alignment of the two tracers is expected. UV-bright components with weak dust continuum could be either metal-poor star-forming regions with little dust buildup or regions in which stellar feedback has removed the dust and gas reservoir. Alternatively, great differences in dust temperature within galaxies could make some star-forming regions appear to have weak dust emission in the 160 μm continuum (the majority of detections) while being bright at $\lesssim$90 μm.

Bowler et al. (2022) and Inami et al. (2022) systematically studied the offsets of dust 160-μm continuum in bright $z \simeq 7$ galaxies. Bowler et al. (2022) identified strong UV-continuum color gradients for galaxies with UV-dust offsets—with redder regions aligned with the dust continuum—confirming the robustness of UV-dust offsets and showing that the UV-bright clumps alone provide a biased view of the full galaxy morphology and colors. Inami et al. (2022) found ∼0.5−1.5 arcsec (2.5–8 kpc) offsets between the rest-UV and FIR emission peaks in galaxies from the REBELS survey and suggest this could imply spatially decoupled phases of obscured and unobscured star formation within a single galaxy or else merging systems. Similar results were found for individual sources (e.g., Hashimoto et al. 2019, Matthee et al. 2019, Schouws et al. 2022, Tamura et al. 2023).

With the launch of JWST and in particular the NIRSpec/IFU (integral field unit) mode, more detailed morphological JWST-ALMA comparisons have become available (e.g., Hashimoto et al. 2023a, Arribas et al. 2024, Jones et al. 2026, Scholtz et al. 2025). As can be seen in **Figure 13**, dust obscuration can introduce significant offsets (∼0.3−0.4 arcsec) between the ALMA and JWST line and continuum tracers—even for emission from the same ion ([OIII] λ88 μm and [OIII] λ5007 Å). In particular, the rest-frame UV emission is concentrated in a number of unobscured clumps, whereas the rest-optical emission lines are highly biased toward a bursty UV-bright region. The gas traced by [CII] λ158 μm and [OIII] λ88 μm, in contrast, shows no evidence for clumpiness related to the rest-UV or optical clumps.

6.1.2. Sizes. Possibly linked to the observed offsets of [CII] and dust continuum is the difference in size measurements between [CII] and UV stellar continuum. Fudamoto et al. (2022) stacked low-resolution observations of star-forming galaxies at $z \sim 4$−7 and found a typical $\gtrsim 2\times$ larger half-light radius of [CII] compared to the stacked UV stellar light. They suggest that MS star-forming galaxies at $z \sim 4$−7 are morphologically dominated by gas rather than stars. Alternatively, if [CII] traces many different phases of the ISM, both obscured and unobscured star-forming regions could be [CII] emitting, naturally increasing the size of the [CII] emitting regions in case of observed offsets between unobscured UV clumps and dust-continuum regions.

Mitsuhashi et al. (2024) use spatially resolved observations of LAEs and LBGs at $z = 4$−6 to show that typical MS star-forming galaxies have dust reservoirs ∼2× more extended than their UV stellar counterparts. This is in strong contrast to SMGs and DSFGs at the same redshift, which typically have very compact, central dust clumps, with UV emission emerging at greater radii (Hodge & da Cunha 2020, and references therein). Ikeda et al. (2025) report that the [CII] sizes of the same galaxies are more extended than the dust in roughly half the sample. They conclude that most of the [CII] extent can be explained by the extended emission from dusty regions; however, emission from extended neutral gas such as that seen in local galaxies could furthermore increase the [CII] sizes.

6.1.3. Halos. The spatial extent of [CII] with respect to the UV stellar light might be conflated by a gas halo around the stellar disk, and for the purposes of this review, we only use the term halo when gas is found on scales of the CGM, e.g., $\gtrsim$10 kpc, which can be separated from the

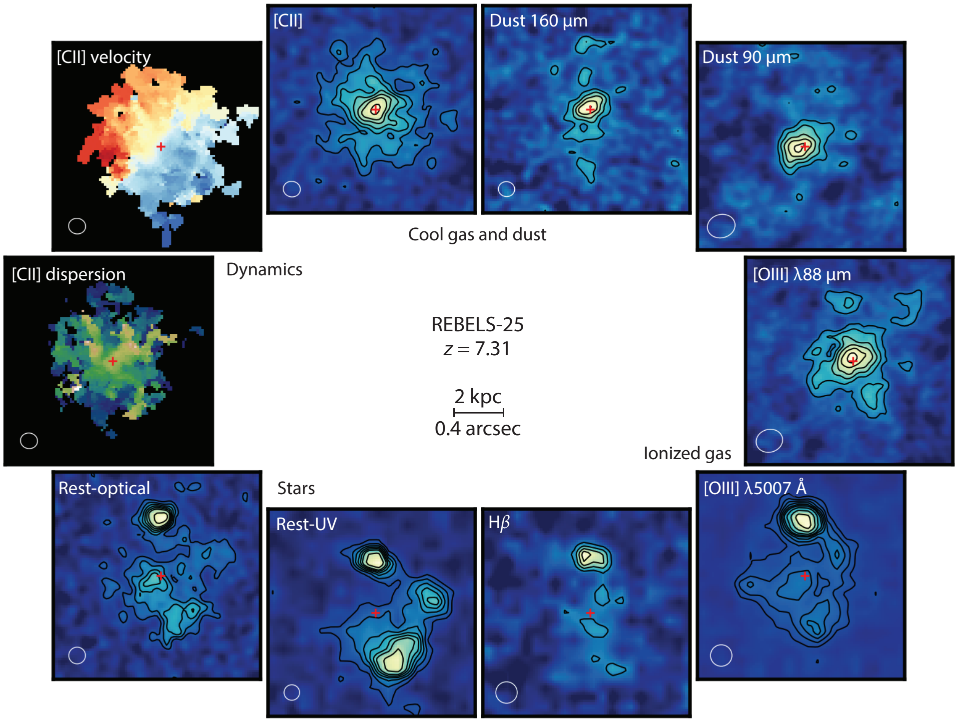

Figure 13

Compilation figure of different galaxy components in the Lyman-break galaxy REBELS-25 ($M_* \sim 10^{10}$ $M_\odot$, $z = 7.3$), inspired by a similar figure of a massive galaxy at $z \sim 2$ in a study by Förster Schreiber & Wuyts (2020). The upper six panels are obtained with Atacama Large Millimeter/submillimeter Array observations of the cool gas ([CII]), including its velocity (rotation) and dispersion (turbulence) of the gas (Rowland et al. 2024), dust (continuum at 90 μm and 160 μm), and hot gas ([OIII] λ88 μm). The lower four panels are obtained with *James Webb Space Telescope* observations using Near Infrared Camera imaging (rest-optical stellar light) and the Near Infrared Spectrograph/*Polarized Radiation Imaging and Spectroscopy Mission* Integral Field Unit (rest-UV stellar light and hot gas seen in Hβ and [OIII] λ5007 Å). For the panels of [CII] dispersion, [CII] velocity, [CII], and Dust 160 μm, data are taken from Rowland et al. (2024) (CC BY 4.0).

ISM-scale emission of [CII]. Using stacking of low-resolution observations, Fujimoto et al. (2019) and Ginolfi et al. (2020) found indications of [CII] halos in $z = 5$–7 and high-SFR $z = 4$–6 galaxies, respectively. Though such a component could be seen as evidence for cold outflows, higher-resolution data are required to rule out multiple close components due to minor and major mergers. Ikeda et al. (2025) studied both individual and stacked high-resolution [CII] emission of $z = 4$–6 galaxies and found no convincing evidence for [CII] halos in either analysis.

By contrast, Akins et al. (2022) studied high-resolution [CII] and [OIII] emission in a $z = 7.13$ lensed galaxy and found clear evidence for a two-component system in [CII] with an ~12-kpc component that is not seen in [OIII]. They argue outflows might explain the origin of the observed halo. Novak et al. (2020) stacked high-redshift quasar host galaxies at $z \gtrsim 6$ and found a two-component profile with an extended ~10-kpc component in both the dust and [CII] and argue that rather than outflows, the extended [CII] component is still tracing the ISM of these extended systems. More high-resolution, high S/N observations are required to settle this discussion and obtain critical insight into the typical CGM conditions of high-redshift galaxies.

6.2. Kinematics

The spectral resolution provided by ALMA and NOEMA is typically higher than that obtained with rest-frame UV and optical spectroscopy with, e.g., JWST. This allows a sensitive probe of the velocity structure of the gas by measuring the peak and shape of FIR emission lines.

6.2.1. Disks and mergers. Velocity gradients were first detected in low angular resolution observations, where disks and mergers are difficult to distinguish. Smit et al. (2018) argued that smooth velocity gradients, combined with compact UV stellar morphologies, in two LBGs at $z \sim 7$ could be evidence of rotation. In contrast, Hashimoto et al. (2019) found a velocity gradient in a $z \sim 7$ LBG that aligned with the two-clump morphology in the UV light and argued for a major merger.

Posses et al. (2023) performed the first high-resolution [CII] analysis of an LBG at $z > 6.5$ and found evidence for a disk (see also Parlanti et al. 2023), accompanied with a minor merger. Furthermore, Rowland et al. (2024) present a kinematically cold gas disk ($v/\sigma \sim 10$) seen in [CII] at $z = 7.3$ in the most FIR-bright LBG from the REBELS survey (see **Figure 13**). The disk dispersion is $\sim 3\times$ ($\sigma \sim 30$ km s^{-1}) higher than observed at $z \sim 0$ in HI/H_2 gas surveys. Such cold gas kinematics are unexpected when extrapolating dynamical measurements at $z = 0-3$ using hot gas tracers, where turbulence increases with redshift and the resulting rotational support decreases (Übler et al. 2019). However, this discrepancy might be explained by the different gas phases traced in these studies, where [CII] is more likely to trace the thin, cold gas disks of galaxies, whereas hot gas is turbulent owing to the impact of stellar feedback (e.g., Rizzo et al. 2021). This is tentatively seen in the chaotic motions traced by [OIII] λ88 μm emission in a lensed LBG at $z = 8.3$ (Tamura et al. 2023), in contrast to the smooth velocity gradient seen in [CII] λ158 μm emission (Bakx et al. 2020). In contrast to the examples of possible disk galaxies at $z > 6.5$, Spilker et al. (2022) present ~100–350-pc scale [CII] gas kinematics of a lensed SMG at $z = 6.9$ and find chaotic motions with highly turbulent clumps ($\sigma \sim 70$–120 km s^{-1}), suggesting both mergers and disk fragmentation could play a role in the bursty nature of this extreme system.

Wang et al. (2024a) present a survey of resolved [CII] emission in 31 $z \sim 7$ quasar host galaxies and find a diversity of kinematics with ~40% having smooth velocity gradients, consistent with rotation, while the rest showed dispersion-dominated, compact, or disturbed kinematics. This is a higher number of rotators than that found in low angular resolution observations of [CII] in LAEs and LBGs at $z \sim 4-6$, where ~40% is classified as mergers and only ~13% as possible rotating disks (Le Fèvre et al. 2020, Jones et al. 2021). However, Lee et al. (2025) find a $50 \pm 9\%$ disk fraction using the high-resolution [CII] observations in a subset of these $z \sim 4-6$ galaxies from the CRISTAL survey. These differences suggest that resolved observations are key to the identification of disks, whereas only modest variations in disk fraction arise due to the different selection criteria of the samples.

6.2.2. Outflows. Similar to the search for [CII] halos, various studies have tried to measure the presence of outflows from the broad, high-velocity components in the integrated and spatially resolved spectra of high-redshift galaxies. Ginolfi et al. (2020) stacked integrated spectra of [CII] in galaxies at $z = 4-6$ and found evidence for a broad component in galaxies with SFR $> 25\ M_{\odot}$ year^{-1}. In contrast, Novak et al. (2020) stack high-redshift quasar host galaxies at $z \gtrsim 6$ and find no evidence for a broad component.

In individual galaxies, Schouws et al. (2023), Hygate et al. (2023), and Fudamoto et al. (2024) report broad components in low angular resolution observations at $z = 6.7$, $z = 7.3$, and $z = 6.2$, respectively, and Herrera-Camus et al. (2021) find evidence for an outflow in resolved observations of a $z = 5.5$ galaxy even if the signature is lost in the integrated spectrum. Hygate et al. (2023) and

Herrera-Camus et al. (2021) find mass-loading factors of $\gtrsim$0.5–1, which are consistent with local relations and predictions from star-formation-driven outflows.

Akins et al. (2022) report a broad [OIII] component found in a brightly lensed LBG at $z =$ 7.1. No such broad component is seen in the [CII] gas, and there is no indication of an extended [OIII] halo (as seen in [CII]; see Section 6.1.3), demonstrating the complexity of hot and cold gas outflows in ALMA observations.

7. DISCUSSION AND FUTURE DIRECTIONS

In Section 1.1, we outlined the underlying changes within the cosmic web in the expanding Universe from $z \sim 0$ to $z \sim 7$ and defined several fundamental questions that we can ask about the ISM of early galaxies. Observationally, ALMA is finding some trends that are broadly consistent with this expected physical picture. For example, line ratios at $z > 6.5$ indicate higher-density ($\sim$10–1,000$\times$) neutral/PDR gas compared to typical $z \sim 0$ galaxies (Section 4.4.3). Furthermore, even in the coldest disks found to date at $z > 6.5$, turbulence is $\sim$3$\times$ higher than that observed in the local Universe (Section 6.2.1). Despite these changes, the relation between the gas traced by [CII] λ158 μm and the SFR stays roughly constant over 13 billion years of cosmic time, suggesting the basic scaling relations fundamental to the star-formation process could already be in place in the EoR (Section 4.2).

Arguably some of the most notable surprises are the evidence for very early metal buildup out to $z \sim 14$ (Sections 4.1 and 4.3.2) and the rapid dust buildup given the modest contribution of AGB stars at early times (Section 5.5). Intriguingly, scaling relations suggest that dust properties appear to evolve little from $z \sim 7$ to today, although the degree of dust-obscured star formation is lower at high redshift (Sections 5.1 and 5.3).

ALMA is only starting to scratch the surface when it comes to constraining the ISM properties that will allow ionizing photons to escape into the IGM. However, interesting results have emerged that suggest that even though most galaxies studied with ALMA to date have modest obscuration fraction (Section 5.1), ALMA traces diffuse highly ionized gas outside of the dense star-forming regions (Section 4.3.2), possibly suggesting a lower covering factor of the PDRs that allows ionizing photons to escape through low-density channels (Section 4.3.3).

In the next decade, ALMA has mapped out high-priority upgrades to the telescope in the ALMA2030 Development Roadmap. ALMA's frequency coverage will be completed with the installation of ALMA band 2 (starting observations in October 2026), which increases the number of CO transitions that can be accessed at high redshift (see **Figure 3**). Top priority for ALMA2030 is the WSU (Wideband Sensitivity Upgrade), which will cover 4$\times$ larger instantaneous bandwidth than is currently available in any ALMA band. Under development are upgrades to bands 2, 6, and 8, which in particular will increase the continuum imaging speed by at least a factor of three, and 2$\times$ larger instantaneous bandwidth for line-scanning purposes. These upgrades guarantee ALMA will continue cutting edge discoveries in high-redshift galaxy formation beyond 2030.

SUMMARY POINTS

1. Over the past decade, since Atacama Large Millimeter/submillimeter Array (ALMA) has come online, far-infrared (FIR) dust continuum has been detected out to $z = 8.3$, cold gas through [CII] λ158 μm out to $z = 9.1$ and hot gas through [OIII] λ88 μm out to $z = 14.2$. ALMA studies above $z = 6.5$ predominantly target luminous sources ($L > L^*$)

and, therefore, massive systems or small samples of lensed galaxies, due to sensitivity requirements.

2. [CII] λ158 μm correlates well with various cold gas tracers. Meanwhile the $z = 0$ SFR (star-formation rate)–[CII] relation is already broadly in place at $z \simeq 7$, suggesting the integrated Kennicutt–Schmidt relation might already be in place, and star-formation efficiency remains roughly constant from the first billion years to the present day.
3. The high [OIII]/[CII] values compared to the local general galaxy population are linked to burstiness of the star-formation history. Elevated [OIII]/SFR values suggest relatively high metal enrichment in bright galaxies out to $z > 11$, possibly in combination with a low covering factor of the PDR, such that star-forming regions leak ionizing photons out to great distances.
4. Dust emission is more common in massive galaxies, as revealed by the trend in $f_{\rm obs}$ with stellar mass from fitting to the rest-optical. Modeling the distribution functions in the FIR lead to estimates of the cosmic star-formation rate density, which shows that >10% of the SFR density at $z \simeq 7$ is obscured.
5. Scaling relations such as IRX–β appear consistent with local relations. Dust temperature shows a large scatter, but the average temperature appears to be moderately elevated as compared to the local Universe ($T_{\rm d} \sim 45$ K).
6. Dust masses compared to the stellar mass suggest that rapid dust enrichment occurs, likely from supernovae with little dust destruction.
7. In individual sources, cold disks are already in existence at $z = 7$, with their gas disks being more extended and smooth than their rest-frame UV and optical counterparts.

FUTURE ISSUES

1. ALMA will continue to push the redshift frontier in terms of spectroscopic line confirmations, given that bright rest-frame optical lines move out of the *James Webb Space Telescope* (JWST)/NIRSpec (Near Infrared Spectrograph) wavelength coverage above $z > 12$, whereas bright lines such as [OIII] λ88 μm, [CII] λ158 μm, and [OI] 63 μm either stay visible in high-transmission bands of ALMA or move into them at these redshifts.
2. With an increase in bright galaxies confirmed at the highest redshifts, new lines become accessible that will constrain interstellar medium properties, such as [OIII] λ52 μm, [OI] λ63 μm, and [NIII] λ57 μm, probing ionized and neutral gas density and abundance patterns.
3. ALMA upgrades will dramatically improve line scanning and enable dust detections or upper limits at increasingly high redshift, constraining the timescale available for dust grain production.
4. The FIR spectral energy distribution will continue to be refined with multiband ALMA observations, constraining the dust temperature and emissivity and, hence, the IR luminosity and dust mass. In parallel, observations with JWST will determine the dust properties via measurements of the attenuation curve, dust bump, and Balmer ratios.

5. With new telescopes like *Euclid* and the *Nancy Grace Roman Space Telescope*, the samples of massive galaxies known at $z > 6.5$ will increase by factors of >1,000, with the low-mass end probed by rare strongly lensed sources. This will provide ideal targets for resolved studies and kinematics for statistical samples of sources within the epoch of reionization.

DISCLOSURE STATEMENT

The authors are not aware of any affiliations, memberships, funding, or financial holdings that might be perceived as affecting the objectivity of this review.

ACKNOWLEDGMENTS

R.B. and R.S. acknowledge support from STFC (Science and Technology Facilities Council) Ernest Rutherford Fellowships (grant numbers ST/T003596/1 and ST/S004831/1). We thank Sander Schouws, Nimisha Kumari, Hiddo Algera, Lucy Rowland, Katherine Ormerod, Matus Rybak, Massimo Stiavelli, Takahiro Morishita, Marusa Bradač, Cosimo Marconcini, Miguel Pereira Santaella, Rychard Bouwens, Robert Crain, and Mauro Stefanon for providing data and/or feedback on the manuscript.

LITERATURE CITED

Akins HB, Fujimoto S, Finlator K, et al. 2022. *Ap. J.* 934:64
Algera HSB, Inami H, De Looze I, et al. 2024a. *MNRAS* 533(3):3098–113
Algera HSB, Inami H, Oesch PA, et al. 2023. *MNRAS* 518(4):6142–57
Algera HSB, Inami H, Sommovigo L, et al. 2024b. *MNRAS* 527(3):6867–87
Algera HSB, Rowland L, Smit R, et al. 2025. Preprint, arXiv:2509.16071 [astro-ph.GA]
Álvarez-Márquez J, Burgarella D, Buat V, et al. 2019. *Astron. Astrophys.* 630:A153
Aravena M, Heintz K, Dessauges-Zavadsky M, et al. 2024. *Astron. Astrophys.* 682:A24
Arribas S, Perna M, Rodríguez Del Pino B, et al. 2024. *Astron. Astrophys.* 688:A146
Bakx TJLC, Sommovigo L, Carniani S, et al. 2021. *MNRAS* 508:L58–63
Bakx TJLC, Tamura Y, Hashimoto T, et al. 2020. *MNRAS* 493(3):4294–307
Bakx TJLC, Zavala JA, Mitsuhashi I, et al. 2023. *MNRAS* 519(4):5076–85
Barrufet L, Oesch PA, Bouwens R, et al. 2023. *MNRAS* 522(3):3926–34
Bate MR. 2025. *MNRAS* 537(2):752–78
Béthermin M, Fudamoto Y, Ginolfi M, et al. 2020. *Astron. Astrophys.* 643:A2
Bouwens R, González-López J, Aravena M, et al. 2020. *Ap. J.* 902(2):112
Bouwens RJ, Aravena M, Decarli R, et al. 2016. *Ap. J.* 833:72
Bouwens RJ, Smit R, Schouws S, et al. 2022. *Ap. J.* 931(2):160
Bowler RAA, Bourne N, Dunlop JS, et al. 2018. *MNRAS* 481(2):1631–44
Bowler RAA, Cullen F, McLure RJ, et al. 2022. *MNRAS* 510(4):5088–101
Bowler RAA, Inami H, Sommovigo L, et al. 2024. *MNRAS* 527(3):5808–28
Bradač M, Garcia-Appadoo D, Huang KH, et al. 2017. *Ap. J. Lett.* 836:L2
Calzetti D, Armus L, Bohlin RC, et al. 2000. *Ap. J.* 533(2):682–95
Calzetti D, Kinney AL, Storchi-Bergmann T. 1994. *Ap. J.* 429:582–601
Cameron AJ, Katz H, Rey MP, Saxena A. 2023. *MNRAS* 523(3):3516–25
Capak PL, Carilli C, Jones G, et al. 2015. *Nature* 522(7557):455–58
Carilli CL, Walter F. 2013. *Annu. Rev. Astron. Astrophys.* 51:105–61
Carniani S, Ferrara A, Maiolino R, et al. 2020. *MNRAS* 499(4):5136–50
Carniani S, Hainline K, D'Eugenio F, et al. 2024. *Nature* 633(8029):318–22
Carvajal R, Bauer FE, Bouwens RJ, et al. 2020. *Astron. Astrophys.* 633:A160

Casey CM. 2012. *MNRAS* 425(4):3094–103
Casey CM, Narayanan D, Cooray A. 2014. *Phys. Rep.* 541(2):45–161
Castellano M, Napolitano L, Fontana A, et al. 2024. *Ap. J.* 972(2):143
Cescon K, Hodge JA, Boogaard LA, et al. 2026. *MNRAS* 549(3):stag924
Chabrier G. 2003. *Publ. Astron. Soc. Pac.* 115(809):763–95
Ciesla L, Adscheid S, Magnelli B, et al. 2025. *Astron. Astrophys.* 700:A277
Cormier D, Madden SC, Lebouteiller V, et al. 2015. *Astron. Astrophys.* 578:A53
Crain RA, van de Voort F. 2023. *Annu. Rev. Astron. Astrophys.* 61:473–515
Curtis-Lake E, Carniani S, Cameron A, et al. 2023. *Nat. Astron.* 7:622–32
da Cunha E, Groves B, Walter F, et al. 2013. *Ap. J.* 766:13
Dayal P, Ferrara A. 2018. *Phys. Rep.* 780:1–64
De Looze I, Cormier D, Lebouteiller V, et al. 2014. *Astron. Astrophys.* 568:A62
Decarli R, Aravena M, Boogaard L, et al. 2020. *Ap. J.* 902(2):110
Decarli R, Díaz-Santos T. 2025. *Astron. Astrophys. Rev.* 33:4
Decarli R, Pensabene A, Venemans B, et al. 2022. *Astron. Astrophys.* 662:A60
Dessauges-Zavadsky M, Ginolfi M, Pozzi F, et al. 2020. *Astron. Astrophys.* 643:A5
Di Cesare C, Graziani L, Schneider R, et al. 2023. *MNRAS* 519(3):4632–50
Draine BT. 2003. *Annu. Rev. Astron. Astrophys.* 41:241–89
Dunlop JS, McLure RJ, Biggs AD, et al. 2017. *MNRAS* 466:861–83
Esmerian CJ, Gnedin NY. 2024. *Ap. J.* 968(2):113
Faisst AL, Fudamoto Y, Oesch PA, et al. 2020a. *MNRAS* 498(3):4192–204
Faisst AL, Schaerer D, Lemaux BC, et al. 2020b. *Ap. J. Suppl. Ser.* 247(2):61
Fan X, Bañados E, Simcoe RA. 2023. *Annu. Rev. Astron. Astrophys.* 61:373–426
Ferrara A, Sommovigo L, Dayal P, et al. 2022. *MNRAS* 512:58–72
Fisher R, Bowler RAA, Stefanon M, et al. 2025. *MNRAS* 539:109–26
Förster Schreiber NM, Wuyts S. 2020. *Annu. Rev. Astron. Astrophys.* 58:661–725
Fudamoto Y, Inoue AK, Bouwens R, et al. 2025. Preprint, arXiv:2504.03831 [astro-ph.GA]
Fudamoto Y, Inoue AK, Coe D, et al. 2024. *Ap. J.* 961:71
Fudamoto Y, Oesch PA, Faisst A, et al. 2020. *Astron. Astrophys.* 643:A4
Fudamoto Y, Oesch PA, Schouws S, et al. 2021. *Nature* 597(7877):489–92
Fudamoto Y, Smit R, Bowler RAA, et al. 2022. *Ap. J.* 934(2):144
Fujimoto S, Bezanson R, Labbe I, et al. 2025. *Ap. J. Suppl. Ser.* 278(2):45
Fujimoto S, Brammer GB, Watson D, et al. 2022. *Nature* 604(7905):261–65
Fujimoto S, Finkelstein SL, Burgarella D, et al. 2023. *Ap. J.* 955(2):130
Fujimoto S, Oguri M, Brammer G, et al. 2021. *Ap. J.* 911(2):99
Fujimoto S, Ouchi M, Ferrara A, et al. 2019. *Ap. J.* 887(2):107
Fujimoto S, Ouchi M, Nakajima K, et al. 2024. *Ap. J.* 964(2):146
Galliano F, Galametz M, Jones AP. 2018. *Annu. Rev. Astron. Astrophys.* 56:673–713
Giménez-Arteaga C, Oesch PA, Brammer GB, et al. 2023. *Ap. J.* 948(2):126
Ginolfi M, Jones GC, Béthermin M, et al. 2020. *Astron. Astrophys.* 633:A90
González-López J, Novak M, Decarli R, et al. 2020. *Ap. J.* 897:91
González-López J, Riechers DA, Decarli R, et al. 2014. *Ap. J.* 784(2):99
Gruppioni C, Béthermin M, Loiacono F, et al. 2020. *Astron. Astrophys.* 643:A8
Gullberg B, De Breuck C, Vieira JD, et al. 2015. *MNRAS* 449(3):2883–900
Gullberg B, Swinbank AM, Smail I, et al. 2018. *Ap. J.* 859:12
Hailey-Dunsheath S, Nikola T, Stacey GJ, et al. 2010. *Ap. J. Lett.* 714:L162–66
Harikane Y, Inoue AK, Mawatari K, et al. 2022. *Ap. J.* 929:1
Harikane Y, Ouchi M, Inoue AK, et al. 2020. *Ap. J.* 896(2):93
Harikane Y, Sanders RL, Ellis R, et al. 2025. *Ap. J.* 993(2):204
Harshan A, Tripodi R, Martis NS, et al. 2024. *Ap. J. Lett.* 977(2):L36
Hashimoto T, Álvarez-Márquez J, Fudamoto Y, et al. 2023a. *Ap. J. Lett.* 955:L2
Hashimoto T, Inoue AK, Mawatari K, et al. 2019. *Publ. Astron. Soc. Jpn.* 71(4):71

Hashimoto T, Inoue AK, Sugahara Y, et al. 2023b. *Ap. J.* 952:48
Hashimoto T, Laporte N, Mawatari K, et al. 2018. *Nature* 557(7705):392–95
Heintz KE, Oesch PA, Aravena M, et al. 2022. *Ap. J. Lett.* 934(2):L27
Heintz KE, Watson D, Oesch PA, et al. 2021. *Ap. J.* 922(2):147
Herrera-Camus R, Bolatto A, Smith JD, et al. 2016. *Ap. J.* 826(2):175
Herrera-Camus R, Förster Schreiber N, Genzel R, et al. 2021. *Astron. Astrophys.* 649:A31
Herrera-Camus R, González-López J, Förster Schreiber N, et al. 2025. *Astron. Astrophys.* 699:A80
Hirashita H, Ferrara A, Dayal P, Ouchi M. 2014. *MNRAS* 443(2):1704–12
Hodge JA, da Cunha E. 2020. *R. Soc. Open Sci.* 7(12):200556
Hygate APS, Hodge JA, da Cunha E, et al. 2023. *MNRAS* 524(2):1775–95
Ikeda R, Ki Tadaki, Mitsuhashi I, et al. 2025. *Astron. Astrophys.* 693:A237
Inami H, Algera HSB, Schouws S, et al. 2022. *MNRAS* 515(3):3126–43
Inoue AK, Tamura Y, Matsuo H, et al. 2016. *Science* 352(6293):1559–62
Ishii N, Hashimoto T, Ferkinhoff C, et al. 2025. *Publ. Astron. Soc. Jpn.* 77:139–48
Isobe Y, Ouchi M, Nakajima K, et al. 2023. *Ap. J.* 956(2):139
Jarugula S, Vieira JD, Weiss A, et al. 2021. *Ap. J.* 921:97
Jones GC, Bowler R, Bunker AJ, et al. 2026. *MNRAS* 547(2):stag336
Jones GC, Vergani D, Romano M, et al. 2021. *MNRAS* 507(3):3540–63
Jones T, Sanders R, Roberts-Borsani G, et al. 2020. *Ap. J.* 903(2):150
Kaasinen M, van Marrewijk J, Popping G, et al. 2023. *Astron. Astrophys.* 671:A29
Kaasinen M, Venemans B, Harrington KC, et al. 2024. *Astron. Astrophys.* 684:A33
Kennicutt RC Jr., Evans NJ. 2012. *Annu. Rev. Astron. Astrophys.* 50:531–608
Khusanova Y, Bethermin M, Le Fèvre O, et al. 2021. *Astron. Astrophys.* 649:A152
Killi M, Watson D, Fujimoto S, et al. 2023. *MNRAS* 521(2):2526–34
Knudsen KK, Richard J, Kneib JP, et al. 2016. *MNRAS* 462:L6–10
Knudsen KK, Watson D, Frayer D, et al. 2017. *MNRAS* 466:138–46
Laporte N, Bauer FE, Troncoso-Iribarren P, et al. 2017. *Astron. Astrophys.* 604:A132
Le Fèvre O, Béthermin M, Faisst A, et al. 2020. *Astron. Astrophys.* 643:A1
Lee LL, Förster Schreiber NM, Herrera-Camus R, et al. 2025. *Astron. Astrophys.* 701:A260
Leśniewska A, Michałowski MJ. 2019. *Astron. Astrophys.* 624:L13
Lewis JSW, Ocvirk P, Dubois Y, et al. 2023. *MNRAS* 519(4):5987–6007
Li J, Venemans BP, Walter F, et al. 2022. *Ap. J.* 930:27
Liang L, Feldmann R, Hayward CC, et al. 2021. *MNRAS* 502(3):3210–41
Liang L, Feldmann R, Kereš D, et al. 2019. *MNRAS* 489:1397–422
Litke KC, Marrone DP, Aravena M, et al. 2022. *Ap. J.* 928(2):179
Litke KC, Marrone DP, Aravena M, et al. 2023. *Ap. J.* 949(2):87
Liu FY, Dunlop JS, McLure RJ, et al. 2026. *MNRAS* 545(2):staf1961
Loiacono F, Decarli R, Gruppioni C, et al. 2021. *Astron. Astrophys.* 646:A76
Lower S, Narayanan D, Hu CY, Privon GC. 2024. *Ap. J.* 965(2):123
Ma X, Hayward CC, Casey CM, et al. 2019. *MNRAS* 487(2):1844–64
Ma Z, Sun B, Cheng C, et al. 2024. *Ap. J.* 975:87
Madau P, Dickinson M. 2014. *Annu. Rev. Astron. Astrophys.* 52:415–86
Madden SC, Cormier D, Hony S, et al. 2020. *Astron. Astrophys.* 643:A141
Madden SC, Rémy-Ruyer A, Galametz M, et al. 2013. *Publ. Astron. Soc. Pac.* 125(928):600–35
Magnelli B, Adscheid S, Wang TM, et al. 2024. *Astron. Astrophys.* 688:A55
Maiolino R, Carniani S, Fontana A, et al. 2015. *MNRAS* 452:54–68
Mancini M, Schneider R, Graziani L, et al. 2016. *MNRAS* 462(3):3130–45
Matthee J, Sobral D, Boogaard LA, et al. 2019. *Ap. J.* 881(2):124
Mauerhofer V, Dayal P. 2023. *MNRAS* 526(2):2196–209
Meurer GR, Heckman TM, Calzetti D. 1999. *Ap. J.* 521:64–80
Mitsuhashi I, Harikane Y, Bauer FE, et al. 2024. *Ap. J.* 971(2):161
Molyneux SJ, Smit R, Schaerer D, et al. 2022. *MNRAS* 512:535–43

Nagao T, Maiolino R, Marconi A, Matsuhara H. 2011. *Astron. Astrophys.* 526:A149
Narayanan D, Conroy C, Davé R, et al. 2018. *Ap. J.* 869:70
Narayanan D, Stark DP, Finkelstein SL, et al. 2025. *Ap. J.* 982:7
Novak M, Bañados E, Decarli R, et al. 2019. *Ap. J.* 881:63
Novak M, Venemans BP, Walter F, et al. 2020. *Ap. J.* 904(2):131
Ota K, Walter F, Ohta K, et al. 2014. *Ap. J.* 792:34
Ouchi M, Ellis R, Ono Y, et al. 2013. *Ap. J.* 778(2):102
Ouchi M, Ono Y, Shibuya T. 2020. *Annu. Rev. Astron. Astrophys.* 58:617–59
Pallottini A, Ferrara A, Gallerani S, et al. 2022. *MNRAS* 513(4):5621–41
Parlanti E, Carniani S, Pallottini A, et al. 2023. *Astron. Astrophys.* 673:A153
Peng B, Lamarche C, Stacey GJ, et al. 2021. *Ap. J.* 908(2):166
Pentericci L, Carniani S, Castellano M, et al. 2016. *Ap. J. Lett.* 829:L11
Pereira-Santaella M, Rigopoulou D, Farrah D, et al. 2017. *MNRAS* 470:1218–32
Pineda JL, Langer WD, Velusamy T, Goldsmith PF. 2013. *Astron. Astrophys.* 554:A103
Popping G. 2023. *Astron. Astrophys.* 669:L8
Popping G, Puglisi A, Norman CA. 2017a. *MNRAS* 472(2):2315–33
Popping G, Somerville RS, Galametz M. 2017b. *MNRAS* 471(3):3152–85
Posses AC, Aravena M, González-López J, et al. 2023. *Astron. Astrophys.* 669:A46
Ramambason L, Lebouteiller V, Madden SC, et al. 2024. *Astron. Astrophys.* 681:A14
Reddy NA, Topping MW, Sanders RL, et al. 2023. *Ap. J.* 952(2):167
Rizzo F, Vegetti S, Fraternali F, et al. 2021. *MNRAS* 507(3):3952–84
Robertson BE. 2022. *Annu. Rev. Astron. Astrophys.* 60:121–58
Rowland LE, Hodge J, Bouwens R, et al. 2024. *MNRAS* 535(3):2068–91
Rybak M, Lemsom L, Lundgren A, et al. 2023. *Res. Notes Am. Astron. Soc.* 7(9):188
Salim S, Narayanan D. 2020. *Annu. Rev. Astron. Astrophys.* 58:529–75
Savage BD, Sembach KR. 1996. *Annu. Rev. Astron. Astrophys.* 34:279–330
Schaerer D, Boone F, Zamojski M, et al. 2015. *Astron. Astrophys.* 574:A19
Schaerer D, Ginolfi M, Béthermin M, et al. 2020. *Astron. Astrophys.* 643:A3
Schneider R, Maiolino R. 2024. *Astron. Astrophys. Rev.* 32:2
Scholtz J, Curti M, D'Eugenio F, et al. 2025. *MNRAS* 539(3):2463–84
Schouws S, Bouwens R, Smit R, et al. 2023. *Ap. J.* 954:103
Schouws S, Bouwens RJ, Ormerod K, et al. 2025. *Ap. J.* 988:19
Schouws S, Stefanon M, Bouwens R, et al. 2022. *Ap. J.* 928:31
Schreiber C, Elbaz D, Pannella M, et al. 2018. *Astron. Astrophys.* 609:A30
Shivaei I, Alberts S, Florian M, et al. 2024. *Astron. Astrophys.* 690:A89
Simpson JM, Smail I, Swinbank AM, et al. 2017. *Ap. J.* 839:58
Smit R, Bouwens RJ, Carniani S, et al. 2018. *Nature* 553(7687):178–81
Smit R, Bouwens RJ, Franx M, et al. 2015. *Ap. J.* 801(2):122
Smit R, Bouwens RJ, Labbé I, et al. 2014. *Ap. J.* 784:58
Solomon PM, Vanden Bout PA. 2005. *Annu. Rev. Astron. Astrophys.* 43:677–725
Somerville RS, Davé R. 2015. *Annu. Rev. Astron. Astrophys.* 53:51–113
Sommovigo L, Algera H. 2025. *MNRAS* 540(4):3693–708
Sommovigo L, Ferrara A, Carniani S, et al. 2021. *MNRAS* 503(4):4878–91
Sommovigo L, Ferrara A, Pallottini A, et al. 2022. *MNRAS* 513(3):3122–35
Spilker JS, Hayward CC, Marrone DP, et al. 2022. *Ap. J. Lett.* 929:L3
Stark DP. 2016. *Annu. Rev. Astron. Astrophys.* 54:761–803
Sugahara Y, Inoue AK, Fudamoto Y, et al. 2022. *Ap. J.* 935(2):119
Sugahara Y, Inoue AK, Hashimoto T, et al. 2021. *Ap. J.* 923:5
Sun F, Wang F, Yang J, et al. 2025. *Ap. J.* 980:12
Swinbank AM, Karim A, Smail I, et al. 2012. *MNRAS* 427(2):1066–74
Tamura Y, Bakx TJLC, Inoue AK, et al. 2023. *Ap. J.* 952:9
Tamura Y, Mawatari K, Hashimoto T, et al. 2019. *Ap. J.* 874:27

Triani DP, Sinha M, Croton DJ, et al. 2020. *MNRAS* 493(2):2490–505
Tripodi R, Feruglio C, Kemper F, et al. 2023. *Ap. J. Lett.* 946(2):L45
Übler H, Genzel R, Wisnioski E, et al. 2019. *Ap. J.* 880:48
Usui M, Mawatari K, Álvarez-Márquez J, et al. 2025. *Ap. J. Lett.* 991(2):L38
Valentino F, Fujimoto S, Giménez-Arteaga C, et al. 2024. *Astron. Astrophys.* 685:A138
Vallini L, Gallerani S, Ferrara A, et al. 2015. *Ap. J.* 813:36
van Leeuwen IF, Bouwens RJ, Hodge JA, et al. 2025. *MNRAS* 542(2):1388–402
van Leeuwen IF, Bouwens RJ, van der Werf PP, et al. 2024. *MNRAS* 534(3):2062–85
Veilleux S, Maiolino R, Bolatto AD, Aalto S. 2020. *Astron. Astrophys. Rev.* 28:2
Venemans BP, Walter F, Decarli R, et al. 2017. *Ap. J.* 845(2):154
Venemans BP, Walter F, Neeleman M, et al. 2020. *Ap. J.* 904(2):130
Viero MP, Sun G, Chung DT, et al. 2022. *MNRAS* 516:L30–34
Vijayan AP, Clay SJ, Thomas PA, et al. 2019. *MNRAS* 489(3):4072–89
Vijayan AP, Wilkins SM, Lovell CC, et al. 2022. *MNRAS* 511(4):4999–5017
Villanueva V, Herrera-Camus R, González-López J, et al. 2024. *Astron. Astrophys.* 691:A133
Walter F, Decarli R, Aravena M, et al. 2016. *Ap. J.* 833:67
Wang F, Yang J, Fan X, et al. 2024a. *Ap. J.* 968:9
Wang F, Yang J, Hennawi JF, et al. 2024b. *Ap. J. Lett.* 962:L11
Ward BA, Eales SA, Ivison RJ, Arumugam V. 2024. *MNRAS* 530(4):4887–901
Watson D, Christensen L, Knudsen KK, et al. 2015. *Nature* 519(7543):327–30
Whitaker KE, Pope A, Cybulski R, et al. 2017. *Ap. J.* 850(2):208
Willott CJ, Carilli CL, Wagg J, Wang R. 2015. *Ap. J.* 807(2):180
Witstok J, Jones GC, Maiolino R, et al. 2023. *MNRAS* 523(2):3119–32
Witstok J, Smit R, Baker WM, et al. 2026. *Open J. Astrophys.* 9(January). **https://doi.org/10.33232/001c.155261**
Witstok J, Smit R, Maiolino R, et al. 2022. *MNRAS* 515(2):1751–73
Wolfire MG, Vallini L, Chevance M. 2022. *Annu. Rev. Astron. Astrophys.* 60:247–318
Yoon I, Carilli CL, Fujimoto S, et al. 2023. *Ap. J.* 950:61
Zanella A, Daddi E, Magdis G, et al. 2018. *MNRAS* 481(2):1976–99
Zavala JA, Bakx T, Mitsuhashi I, et al. 2024. *Ap. J. Lett.* 977:L9
Zavala JA, Casey CM, Manning SM, et al. 2021. *Ap. J.* 909(2):165
Zhao Y, Liu J, Zhang ZY, Bisbas TG. 2024. *Ap. J.* 977:46
Zimmerman DT, Narayanan D, Whitaker KE, Davé R. 2024. *Ap. J.* 973(2):146